Identifying Quasi-periodic Variability Using Multivariate Empirical Mode Decomposition: a Case of the Tropical Pacific

Lina Boljka[1], Nour-Eddine Omrani[1], and Noel S. Keenlyside[1]

[1]Geophysical Institute, University of Bergen and Bjerknes Centre for Climate Research, Bergen, Norway

Correspondence: Lina Boljka (lina.boljka@uib.no), Nour-Eddine Omrani (noureddine.omrani@uib.no)

Abstract. A variety of statistical tools have been used in climate science to gain a better understanding of the climate system's variability on various temporal and spatial scales. However, these tools are mostly linear, stationary or both. In this study, we use a recently developed nonlinear and nonstationary multivariate timeseries analysis tool – multivariate empirical mode decomposition (MEMD). MEMD is a powerful tool for objectively identifying (intrinsic) timescales of variability within a given spatio-temporal system without any timescale pre-selection. Additionally, a red noise significance test is developed to robustly extract quasi-periodic modes of variability. We apply these tools to reanalysis and observational data of the tropical Pacific. This reveals a quasi-periodic variability in the tropical Pacific on timescales ~1.5-4.5 years, which is consistent with El Niño Southern Oscillation (ENSO) – one of the most prominent quasi-periodic modes of variability in the Earth's climate system. The approach successfully confirms the well known out-of-phase relationship of tropical Pacific mean thermocline depth with ~~sea-surface-temperature~~ sea surface temperature in the eastern tropical Pacific (recharge-discharge process). Furthermore, we find a co-variability between zonal wind stress in the western tropical Pacific and the tropical Pacific mean thermocline depth, which only occurs on the quasi-periodic timescale. MEMD coupled with a red noise test can therefore successfully extract (nonstationary) quasi-periodic variability from the spatio-temporal data, and could be used in the future for identifying potential (new) relationships between different variables in the climate system.

1 Introduction

The climate system is a highly complex system consisting of variability across many different timescales (e.g., Baede et al., 2001). Among these, quasi-periodic patterns of variability are important as they can be leveraged for medium-to-long range predictions (e.g., Mariotti et al., 2018, 2020; L'Heureux et al., 2020). Statistical tools have been particularly helpful in identifying quasi-periodic variability.

The following are typical statistical tools used for exploring the patterns of variability on different temporal and/or spatial scales (Broomhead et al., 1987; Hasselmann, 1988; Penland and Sardeshmukh, 1995; Ghil et al., 2002; Huang et al., 1998; Ghil et al., 2002; Froyland et al., 2021): Fourier transform (FFT), wavelet transform, principal component analysis (PCA), (multi-channel) singular spectrum analysis ((M)SSA), principal oscillation patterns (POPs), linear inverse model (LIM) or even nonlinear Laplacian spectral analysis. However, these methods do not necessarily have a multivariate extension, and/or are either stationary, linear or both. Additionally, some methods, such as (M)SSA, require specification of a window over

which quasi-periodic signals are sought, making them somewhat subjective. These can be drawbacks when studying complex, inherently nonlinear, and nonstationary systems, such as the climate system.

Multivariate empirical mode decomposition (MEMD) addresses these drawbacks as it is an analysis tool that is entirely data adaptive, and is designed to extract *nonlinear* and *nonstationary* signals. MEMD is a generalisation of the empirical mode decomposition (EMD; Huang et al., 1998) to multivariate datasets of more than two timeseries (Rehman and Mandic, 2010). EMD is a 1-D timeseries analysis tool that is based on Hilbert transform and takes advantage of the instantaneous frequency, allowing a 'local' extraction of modes of variability. Each mode that the EMD extracts consists of two elements: (1) typical timescale of the mode, i.e., average instantaneous frequency of the mode; and (2) the timeseries of the mode. Beyond this, MEMD extracts timescales *common* to *all* input timeseries (i.e., synchronises signals) and provides modes (patterns) of variability according to these timescales.

Despite their appeal, MEMD and EMD have hardly been used in climate research. EMD and its 1-D extension Ensemble EMD (EEMD; Wu and Huang 2009) have been used for smoothing, filtering, extracting trends, variability, and testing for red noise distribution of climate data (e.g., Duffy, 2004; Wu et al., 2007; Franzke, 2009; Lee and Ouarda, 2011; Qian et al., 2011; Franzke and Woollings, 2011; Franzke, 2012; Ezer and Corlett, 2012; Ezer et al., 2013; Wang and Ren, 2020). MEMD has only been used for an idealised analysis of atmosphere-ocean coupling strength (Alberti et al., 2021). Moreover, neither MEMD ~~or~~ nor EMD have been used for extracting quasi-periodic modes of climate variability.

A major challenge in applying MEMD in climate analysis is that no statistical null hypothesis test for ~~red-noise~~ red noise has been developed. When applied to climate data, MEMD can reveal many modes that are consistent with red (or white) noise. In particular, sea surface temperature (SST) exhibit a red spectrum, because it represents the 'integral' response of the ocean to stochastic higher-frequency atmospheric (e.g., "weather", "white noise") variability (e.g., Hasselmann, 1976; Frankignoul and Hasselmann, 1977). However, there are also patterns of quasi-periodic variability (e.g., repeating every 2-8 years) that reflect more complex climate dynamics. To identify such quasi-periodic variability in the climate system, any analysis would first require a significance test that could distinguish this variability from the red noise. In other words, we seek spectral peaks (modes of variability) that pass the ~~red-noise~~ red noise threshold (Gilman et al. 1963; Madden and Julian 1971; Bretherton et al. 1999, see also section 4, Appendix B2).

In this study, we combine the MEMD method with a red noise test (sections 3, 4) to robustly detect quasi-periodic modes of variability. Thus, MEMD becomes well-suited for analysing nonlinear and nonstationary climate data. It also has the advantage of *objectively* detecting intrinsic timescales *without pre-selecting* or/and filtering for a frequency band (as in, e.g., MSSA), and without any periodic signal or basis of functions specifications (as in, e.g., Fourier transform and wavelet analysis). Since MEMD and (especially) its combination with a red noise test is a new tool in climate science, we test it on a known example of quasi-periodic variability. Namely, we analyse the tropical Pacific atmosphere-ocean variability to extract the El Niño Southern Oscillation (ENSO). In the future, this tool may be used in other spatio-temporal applications, where quasi-periodic variability has not yet been identified.

ENSO is a quasi-periodic phenomenon occurring on (interannual) timescales of 2-8 years (e.g., Philander, 1990; Wang and Fiedler, 2006; Timmermann et al., 2018). ENSO events are ~~characterized~~ characterised by warming tropical Pacific SST

during the development of El Niño (warm phase) and cooling of SST afterwards leading into La Niña (cold phase). These events are typically characterised by ocean-atmosphere interaction, whereby atmospheric changes in winds can lead to changes in the distribution of warm and cold waters in the ocean that in turn impact the atmosphere. ENSO exhibits significant non-linearities, with marked skewness and phase locking to the seasonal cycle (e.g., Stein et al., 2010; Dommenget et al., 2013). It is also non-stationary (e.g., Crespo et al., 2022; Fedorov and Philander, 2000). This complex coupled dynamics is different from red noise and is therefore the focus of the present study.

The manuscript is structured as follows. Section 2 provides description of data used; section 3 describes the EMD and MEMD implementation (Appendix A provides further details); section 4 provides description of the red noise test (Appendix B provides further details); sections 5, 6 identify modes of variability in the tropical Pacific and explore the physical mechanisms relevant on different timescales. Conclusions are given in section 7.

2 Data

We focus on the intrinsic variability of the tropical Pacific and analyse monthly mean data of three different variables relevant for atmosphere-ocean exchange: sea surface temperature (SST) from HadISST observational dataset (Rayner et al., 2003), surface zonal wind stress (τ_x) and thermocline depth (i.e., the depth of the 20°C isotherm) both from SODA2 ocean-reanalysis dataset (Carton and Giese, 2008). These three variables are used to asses the ENSO dynamics as these quantities typically play a leading role in the onset and decay of ENSO events, and are typically used in the oscillator models that explain ENSO dynamics (see section 6 and, e.g., Wang, 2018). The data are analysed in the tropical Pacific (110°E - 65°W, 25°S - 25°N) over the period 1871-2010 for which all datasets are available. Note that surface wind stress and the ocean subsurface data reconstructions in the 19th and early 20th century are less reliable than in the late 20th century due to sparser data coverage, thus the results presented here are only as accurate as these reconstructions can be (Wittenberg, 2004; Crespo et al., 2022). We use the early record data here to show the nonstationarity/nonlinearity of the tropical Pacific variability over the last ∼140 years. The identification of the two main quasi-oscillatory modes (section 5) is also not affected by the inclusion of this data.

The MEMD analysis (section 3) is performed on all fields simultaneously with SST at the highest resolution (1° in latitude and longitude), whereas thermocline depth and τ_x (both 9° resolution in longitude, 5° resolution in latitude) have much lower resolution. This gives greater weight to SST data in the analysis, and less towards the other variables, such that the mode does not change significantly by adding other variables in the analysis (i.e., results below for the SST are similar whether we use SST alone or together with other fields). This choice is made because we are primarily interested in the quasi-periodic behaviour in SST, since SST are used for defining ENSO (e.g., in Niño3 region—see Table 1). SST are also typically smoother than other fields. This is especially true for wind stress, which is strongly affected by the "noisy" atmospheric variability. This ensures that modes that emerge from MEMD analysis are representative of quasi-periodic variability in SST (and thus ENSO), while the rest of the variables are "enslaved" to SST variability. The other variables are added to the MEMD input data to describe the climate dynamics involved in the quasi-periodic SST variability, e.g., ENSO (section 6). Note that MEMD can be sensitive to input data, thus we must carefully consider the input data structure (relevant to a specific study).

Table 1. Tropical Pacific regions used for computing timeseries (see text for details). The right-most column lists the variables that are averaged over specified regions.

Region	Latitude Range	Longitude Range	variable
Niño3	5°S - 5°N	150°W - 90°W	SST
Niño4	5°S - 5°N	160°E - 150°W	zonal wind stress
Niño5	5°S - 5°N	120°E - 140°E	zonal wind stress
Niño6	8°N - 16°N	140°E - 160°E	thermocline depth
Pacific mean	5°S - 5°N	120°E - 90°W	thermocline depth

While the SST, thermocline depth, and τ_x play an important role in the ENSO dynamics, it is specific regions (see Table 1) that have historically been analysed in more detail, for example, in conceptual oscillator models (e.g., Jin, 1997a; Wang, 2018). The timeseries in the specific regions are thus used to assess if MEMD modes on ENSO timescales are consistent with physics described by conceptual oscillator models (section 6). Additionally, analysing such timeseries helps a simpler visualisation of temporal evolution of different variables. Thus, we average τ_x over Niño4 and Niño5 regions separately, thermocline depth over Niño6 region (off-equatorial thermocline depth) and over the tropical Pacific (Pacific mean), and SST over Niño3 region (again, see Table 1; see also Fig. 3 in Wang et al. 1999). Note that regional averages (Table 1) are computed after the MEMD analysis is performed (for details see section 3).

Before performing the analysis, we detrend the data and remove its seasonal cycle, which is done the following way (cf., de la Cámara et al., 2019). First, we calculate 30-year means centered on every 10th year for each individual month. This yields one value for each individual month every 10 years. Then we interpolate between these values (of every 10th year) to obtain yearly time series, again for each individual month. This yields a smooth seasonal cycle that includes a trend and seasonal cycle for every month in the record. Detrended and ~~deseasonalized~~ deseasonalised data are then computed as the difference between the original monthly timeseries and the smooth trend/seasonal cycle. We do this at every grid point and for every variable separately.

This is done to avoid domination of the seasonal cycle or trend in the statistical analysis below, even though the MEMD can generally extract nonlinear trends by itself. Note that this means that we cannot assess the impact of long-term variability or seasonal cycle on ENSO variability in this study, but the latter may still be present indirectly, as ENSO is phase-locked to the seasonal cycle (e.g., Stein et al., 2010; Wengel et al., 2018).

3 (Multivariate) Empirical Mode Decomposition

3.1 MEMD description

115 We employ MEMD to *objectively* identify intrinsic modes of variability in *nonlinear* and *nonstationary* spatio-temporal data. To understand MEMD, it is easier to first consider the simpler implementation of the 1-D version, Empirical Mode Decomposition (EMD), as outlined by Huang et al. (1998):

(i) Local minima and maxima of the input (1-D) timeseries (e.g., see black solid line in Fig. 1) are identified.

(ii) Envelopes are created by interpolating between subsequent maxima (upper envelope, shown as grey dotted line in Fig.
120   1) and between subsequent minima (lower envelope, represented by grey dashed line in Fig. 1).

(iii) An average envelope is obtained by taking the mean of the upper and lower envelopes (depicted by the red solid line in Fig. 1).

(iv) The average envelope is subtracted from the original timeseries data.

(v) The subtracted data, i.e., the original data minus the average envelope, represent the first mode of variability and typically
125   correspond to the highest-frequency signal in the dataset. However, the average envelope can be further analysed.

(vi) Steps (i)-(v) are repeated on the average envelope until only a trend or residual component remains. This occurs when we can no longer find at least two extrema in the dataset, which is a condition that needs to be satisfied by EMD's modes of variability.

The resulting modes of variability (i.e., the output of the EMD analysis), represented by their respective timeseries, are known
130 as intrinsic mode functions (IMFs). The timescale of each IMF is characterised by the time-lapse between two subsequent extrema, and the mean timescale of an IMF represents the average over all time-lapses within its timeseries.

Additionally, each IMF has to satisfy two criteria: (a) the number of extrema and the number of zero-crossings differs at most by one; and (b) the mean value of the envelope of the IMF is zero. Note that the procedure from (i) to (iv) does not necessarily satisfy (a)-(b) immediately, thus an additional sifting process (typically iterative) is used that requires a stopping
135 criteria to ensure physical meaning of the IMFs. The stopping criteria can be based on the standard deviation of each IMF, on the maximum number of iterations, etc., which set tolerance and confidence limits for the IMF (for details see Huang et al., 1998; Rilling et al., 2003; Huang et al., 2003). Ultimately, this process extracts modes of variability that consist of (1) typical timescale of the mode and (2) its timeseries. The modes are automatically ordered from highest/shortest (mode 1) to lowest/longest (last mode) frequency/period. Note that modes that emerge are largely independent with only small correlations
140 between them.

MEMD (Rehman and Mandic, 2010) is a generalisation of the EMD to multivariate datasets of more than two timeseries (for bivariate and trivariate data separate methods exist; Rilling et al. 2007; Rehman and Mandic 2010). The method solves a similar problem as in (i)-(vi) but the mean envelope is computed as (Rehman and Mandic, 2010) "an integral of all the envelopes along
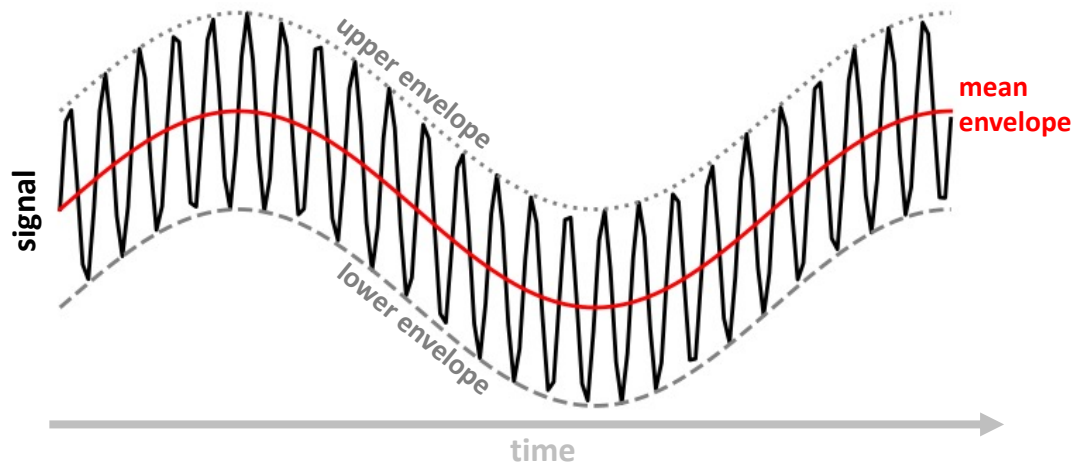
Figure 1. Schematic for obtaining average envelope during EMD process. Black line shows a simple input signal that is a sum of two sine waves (a low frequency and a high frequency wave). Grey dotted and grey dashed lines show upper and lower envelope, respectively. Red line shows average envelope, which represents the low frequency of the input signal. If we remove the average envelope from our input data, we obtain the high frequency signal (e.g., the first mode of EMD).

multiple directions in an N-dimensional space" (i.e., on an N-Sphere). This is much more complex, but the basic idea remains

145   similar to the 1-D method, and the method retains similar stopping criteria for the sifting process. For further details on and visualisations of the method the reader is referred to Rehman and Mandic (2010); Alberti et al. (2021).

     The MEMD ultimately extracts timescales *common* to *all* input timeseries (i.e., synchronises signals; Rehman and Mandic 2010) and provides multivariate IMFs (i.e., the outputs of MEMD method) describing those timescales. The timescales of IMFs are then consistent across the input timeseries — to visualise this, see supplementary Figs. S6-S10, Tables S1-S2, and section

150   S.3 for an idealised example.

     As with all statistical methods, it is important to be aware of the drawbacks associated with the (M)EMD (e.g., Stallone et al., 2020). Similar to other timeseries-filtering methods, (M)EMD can encounter issues at the edges of the timeseries, which can result in "travelling waves" and thus unrealistic peaks in the timeseries (e.g., Stallone et al., 2020). Another common challenge with (M)EMD is the mixing of modes (see below) where a single genuine mode may be split into multiple modes if

155   inappropriate parameters are chosen (e.g., Huang et al., 1999, 2003; Stallone et al., 2020). However, this issue can also arise when there is no clear timescale-separation. To address these challenges, it is crucial to test the physical relevance of the modes of variability identified using (M)EMD and to ensure convergence and stability of the modes through different parameter sweeps that are related to the stopping criteria (see section 3.2). Note that different parameter sweeps may be relevant for different applications.

3.2 MEMD parameter sweep

The code for the MEMD is freely available on Github (https://github.com/mariogrune/MEMD-Python-; similarly for the EMD discussed above: https://github.com/laszukdawid/PyEMD), and the user ultimately only decides about the stopping criteria. These are set to the "fix_h" parameter, following Huang et al. (2003) who suggest that limiting iterations yields better-behaved IMFs than other stopping criteria. We limit the number of iterations to 15 (parameter "n_iter" is 15), though other values were tested and a range for "n_iter" around 5-30 yielded similar results, suggesting some convergence for the *significant* modes of variability (see below).

Note that at higher/lower frequencies we find mode-mixing in our MEMD analysis where timescales are not clear (here, this occurs on timescales shorter than about 8 months and longer than about 700 months), and also with larger number of iterations. These modes are not detected as different from ~~red-noise~~ red noise (see sections 4, 5 for more details). However, the significant modes of variability on interannual timescales that are of interest here are largely unaffected by this (section 5).

3.3 Obtaining modes of variability via MEMD

As mentioned in section 2, we use 3-D data relevant for ENSO dynamics, i.e., $\mathbf{A}(L_t, L_y, L_x)$ (with L_t length of time dimension, L_y length of latitude dimension, L_x length of longitude dimension, $\mathbf{A}$ as the selected variable(s)/field(s); bold letters represent two- or three-dimensional arrays) as basis for the MEMD analysis, which is done the following way.

(i) First, we remove the smooth trend/seasonal cycle (described above; see also de la Cámara et al., 2019) from $\mathbf{A}$ to get a temporal anomaly, $\mathbf{A}'$.

(ii) We divide data by their standard deviations (σ; done separately for each variable and at each grid point).

(iii) Since we use more than one variable (i.e., SST, surface wind stress, thermocline depth) in the analysis, we concatenate (denoted with $\oplus$) the different variables in their spatial dimensions, i.e., we get $\mathbf{A}'(L_t, L_y = L_{y1} \oplus L_{y2} \oplus ..., L_x = L_{x1} \oplus L_{x2} \oplus ...)$ (with subscripts 1,2,... representing spatial dimensions of the different variables).

(iv) Then, we reduce the dimensionality by computing spatial patterns (empirical orthogonal functions, EOFs) and their timeseries (principal components, PCs) via singular value decomposition (SVD).

(v) Finally, we only retain the first 20 PCs that explain the majority of the variance in the field $\mathbf{A}'$. The PCs are then used as input data for the MEMD algorithm (for further details ~~of~~ on the whole procedure see Appendix A).

MEMD analysis identifies 21 IMFs that are ordered by frequency from the highest (IMF1) to the lowest (IMF21) with the last 21st mode typically representing a trend, which in our case was already removed (see above). Namely, we find 21 potential intrinsic timescales within the tropical Pacific, i.e., common to all input PCs. This means that we obtain 21 IMFs for each PC-timeseries, i.e., $\mathrm{PC}_m(L_t) = \sum_s \mathrm{IMF}_s(\mathrm{PC}_m(L_t))$ with s IMF-number and m PC-number, where s^{th} IMF of each PC_m has the same timescale (see Table S2). Since we initially obtained PCs via SVD analysis and we thus have corresponding EOF patterns, we can then reconstruct spatio-temporal patterns of variability for each field (i.e., SST, wind stress and thermocline

depth) from PCs and EOFs. As the interest here is in the variability on different timescales, i.e., for each (s^{th}) IMF separately, we can perform this reconstruction for each IMF across all 20 PCs/EOFs, i.e.,

$$\text{IMF}_s^{spatial}(L_t, L_y, L_x) \simeq \sum_m \text{IMF}_s(\text{PC}_m(L_t))\text{EOF}_m(L_x, L_y). \tag{1}$$

Please recall that input data for MEMD analysis were divided by σ, thus for variability of a field in its original units we need to multiply spatio-temporal IMFs by σ.

To compute an index, such as eastern Pacific SST (Niño3), we can average over a latitude-longitude region (Table 1) from spatio-temporal IMFs (Eq. 1) to obtain timeseries of, e.g., eastern Pacific SST (Niño3) for each IMF separately — see supplementary Figs. S6-S10 for timeseries of different variables from Table 1, and Table S1 for their timescales. This yields an index for each IMF (e.g., IMF_s(SST (Niño3)) with s IMF-number) corresponding to an equivalent index computed from input data ($\mathbf{A}'$). The latter is approximately the same as the sum of indices computed from all IMFs, e.g., SST(Niño3)$(L_t) \simeq \sum_s \text{IMF}_s$(SST(Niño3)$(L_t)$).

4 Statistical significance test for climate

Once we have computed the IMFs, we need to test if they are statistically significant. The importance of each IMF can be assessed by computing variance explained of each IMF relative to the input field (e.g., retaining those IMFs that explain more than 0.1% variance) or through other significance tests (e.g., white noise test; Appendix B1; Wu and Huang, 2004). We develop a test for variability that can be distinguished from ~~red-noise~~red noise, as appropriate for studying climate variability (see Introduction).

The red noise test can be performed in different ways (see also section 5.1): (i) we can choose an index of interest and perform a red noise test on its IMFs (see below; Fig. 2) - this can be used when we are interested in quasi-oscillatory behaviour of a specific index (e.g., areal average) we constructed or on a known climate index we wish to test; (ii) more objectively, we can use IMFs of specific PC timeseries (e.g., PC1~~'s IMFs (more objective~~; Fig. S2) ~~;~~ this can be used when we are interested in quasi-oscillatory behaviour of an index that explains a specific amount of variance in a field or region (e.g., tropical Pacific); and (iii) we can test for quasi-periodic variability at each grid point (section 5.1, Fig. 5) ~~; or other. Thus, significance of modes is only relevant for the index/region used in the red noise test calculation.~~ this can be used to identify potential regions of quasi-oscillatory behaviour that have not been identified before. In general, all methods can be used together (as done here) for robustness, but their use will ultimately depend on a specific scientific question.

Here, we first test for potential quasi-periodic variability using SST timeseries that are relevant for (eastern Pacific) ENSO variabilty, i.e., eastern Pacific SST (Niño3) from input data and corresponding eastern Pacific SST (Niño3) from spatio-temporal IMFs (as described in section 3; IMF_s(SST (Niño3))). Then, we compute power spectrum for each timescale/period (i.e., each IMF) by obtaining average squared amplitude of each (s^{th}) IMF (E_s), i.e., $E_s = (\sum_j[\text{IMF}_s(j)]^2)/L_t$ (with L_t length of the timeseries, j each timestep). Average timescale (T_s) of each IMF is computed from instantaneous frequency using Hilbert transform (see text around Eq. B4 in Appendix B1), which yields similar results to computing time lapse between
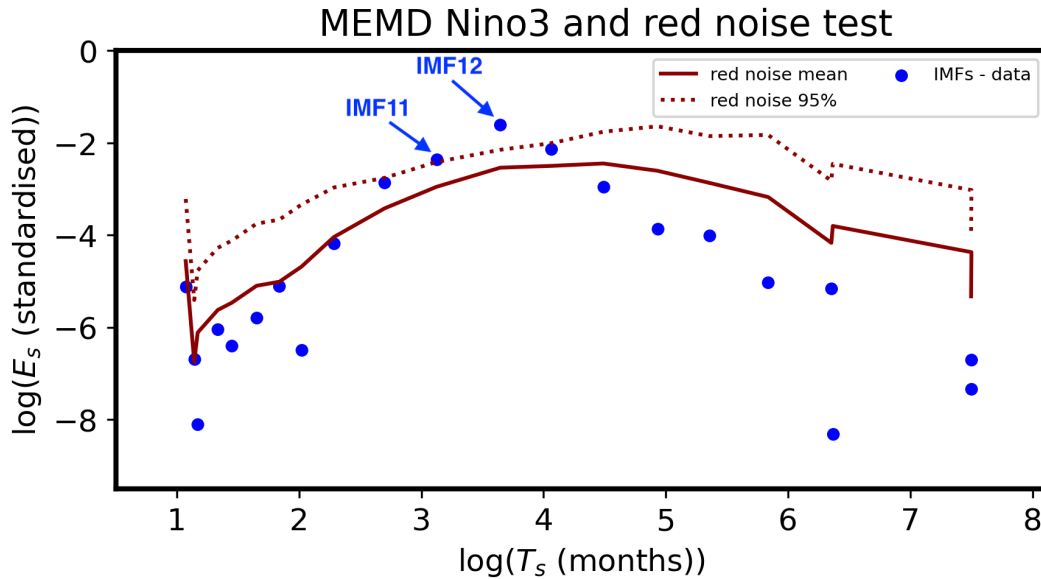
Figure 2. Red noise significance test for spatio-temporal IMFs (from MEMD) via SST averaged over the Niño3 region (for details see text and Appendices A,B). Each blue dot represents average squared amplitude (E_s; Eq. B1) and average period (T_s; in months; for periods of IMFs see Table S1) of each IMF that we have identified within our timeseries/data. Average period is computed from instantaneous frequency obtained via Hilbert transform (see text under Eq. B4). For visualisation purposes we obtain a natural logarithm of both average squared amplitude ($\log_e(E_s)$; y-axis) and average period ($\log_e(T_s)$; x-axis) of each IMF and plot them as a scatter plot (blue dots). Note that the logarithms of periods ($\log_e(T_s)$) are ordered from shortest period (highest frequency; IMF1; left-most blue dot) to longest period (trend; IMF21; right-most blue dot). Red solid line represents the theoretical red spectrum fit (Eqs. 2, B7-B9), red dotted line represents the one-tailed 95th percentile confidence level (via χ^2-test). For further descriptions of the figure see text.

two extrema in the timeseries. E_s is then plotted against T_s (here we use their logarithmic values) to yield the power spectrum plot (blue dots in Fig. 2).

225   The shape of the red noise fit (red solid line in Fig. 2), or rather red noise spectrum for every s^{th} IMF, can be computed from the lag-one autocorrelation of the input data (e.g., eastern Pacific SST (Niño3)) as (cf., Gilman et al. 1963; Kolotkov, D. Y. et al. 2016; for full derivation and further discussion see Appendix B)

$$E_s^{red}(\nu_s) = \frac{1 - r^2}{1 - 2r\cos 2\pi\nu_s + r^2}(\nu_s\alpha_s - \nu_s/\beta_s). \tag{2}$$

E_s^{red} is a theoretical estimate of the (mean) energy of the red noise of sth IMF, $\nu = 1/t$ is frequency, t is time, r is lag-1

230 auto-correlation of input data of eastern Pacific SST (Niño3), $\beta_s = \sqrt{\nu_s/\nu_{s+1}}$ and $\alpha_s = \sqrt{\nu_{s-1}/\nu_s}$, and subscript s represents the sth IMF of frequency ν_s (ordered from highest to lowest frequency).

    E_s^{red} is then scaled so that the variance of the red noise fit is identical to the variance of the spectra computed from the spatio-temporal IMFs (E_s; Eq. (B9); see also, e.g., Madden and Julian 1971; Bretherton et al. 1999). The 95% confidence curve (red dashed line in Fig. 2) is computed by multiplying the red noise fit by χ^2 statistic for a one-sided p-value of 0.05. The

235   number of degrees of freedom for s^{th} IMF is computed as $\text{DoF}_s = E_s L_t (1-r^2)/(1+r^2)$ (for further details see Appendix B2; see also Bretherton et al. 1999; Wu and Huang 2004; Kolotkov, D. Y. et al. 2016). Note that the same procedure (as described above) can be applied to any other timeseries/IMFs.

5   Tropical Pacific modes of variability

As MEMD in conjunction with a ~~red-noise~~ red noise test has not been applied in climate science before, we perform extensive
240   analysis of the method itself (in addition to analysis of ENSO dynamics - see below). Then, we compare it to the basic band-pass filtering (5th order Butterworth filter) and to Fourier transform analysis to ensure consistency with other methods. Please recall that while other spectral methods often require prior knowledge about the spatial/temporal patterns of interest in order to construct appropriate indices, the MEMD method allows for the objective extraction of significant patterns and modes of variability from data without pre-existing knowledge (see also below and Appendices A, B).

245   5.1   Significant modes of variability

We identify two significant modes of variability in the eastern Pacific: the 11th IMF (IMF11) and 12th IMF (IMF12) (pointed out with blue arrows in Fig. 2) with average timescales of ∼23 and ∼39 months (∼2-3 years; see also Table S1), respectively. Their timescales fall well within the the typical ENSO timescale range (2-8 years), as can be identified via a typical power spectrum analysis (Appendix B2, Fig. B3). These timescales (with their uncertainty ranges; see below) are consistent with
250   previously identified quasi-biennial (QB, ∼2 years) and low-frequency/quasi-quadrennial (LF/QQ, ∼4 years) ENSO modes (e.g., Jiang et al., 1995; Allan, 2000; Kim et al., 2003; Keenlyside et al., 2007; Bejarano and Jin, 2008; Jajcay et al., 2018; Froyland et al., 2021).

    The quasi-periodic mode of variability with 39 months average period (IMF12) is more statistically significant (than IMF11). This can be seen in different ways. First, considering the Niño3 index (i.e., eastern Pacific SST in Niño3 region), IMF11 (blue
255   dot) lies only slightly above the 95% red noise threshold (red dashed line), whereas IMF12 lies well above the threshold (Fig. 2). Second, considering the PC1's IMFs (i.e., before we do spatio-temporal reconstruction of IMF-data; Fig. S2), only IMF12 is found to be significant, despite the generally good agreement between the Niño3 index and PC1 of the tropical Pacific SST (e.g., Ashok et al., 2007). Finally, we can perform a red noise test on each grid point of the tropical Pacific (similarly as for specific timeseries shown above) and plot spatial structure of SST together with the significance test (section 6, Figs. 5, S3).
260   This shows that none of the grid points of spatio-temporal IMF11 pass the red noise threshold (Fig. S3), but many grid points of the spatio-temporal IMF12 are significant (not-shaded in grey in Fig. 5).

    Nevertheless, even though IMF11 is marginally statistically significant, the MEMD analysis suggests that there may be two quasi-periodic modes of interannual SST variability in the tropical Pacific region. This agrees with previous results that have identified two statistically significant modes of variability with specific frequencies and distinguished by their dynamics. Note,
265   we also find that the two modes of variability are well separated (in terms of timescale) from the other modes and from each other, as shown by Fig. 2. This ensures no mode-mixing on the quasi-periodic timescales.

On longer timescales, we do not find any behaviour that would be discernible from red noise, suggesting that the lower-frequency range of ENSO (timescales longer than ∼4.5 years) (e.g., Allan, 2000; Jajcay et al., 2018) is better represented by red noise. Recall, however, that any potential oscillatory behaviour on timescales longer than 30-years was removed via detrending. Similarly, we do not find any quasi-periodic modes of variability on shorter timescales. Also, on these longer (> 700 months) and shorter (< 8 months) timescales we find some mode mixing. This is likely a consequence of inputting several different variables (i.e., SST, τ_x, thermocline depth) into MEMD algorithm, where each variable can have different timescales represented. For example, wind stress can be much noisier than SST (or different parts of the tropical Pacific have different variabilities) and can thus lead to identification of several high frequency modes of variability, resulting in mode-mixing (see somewhat overlapping blue dots in Fig. 2).

5.2 Timeseries of significant modes of variability

Above we have established that the Niño3 index in the tropical Pacific exhibits two quasi-periodic modes of variability with average periods ∼2-3 years (via MEMD analysis). We now analyse the associated timeseries of the two IMFs (IMF11 and IMF12) and compare them with a band pass (16-53 months) filtered Niño3 index (Fig. 3).

The period/frequency of the two modes is not constant (i.e., varies in time). Thus, we also specify a range of periods/frequencies for the two modes. The mean periods of IMF11,12 with their 'uncertainty' ranges (in square brackets) are: 23 [16, 33] (IMF11), and 39 [29, 53] (IMF12) months. These ranges are defined based on the 6.7^{th} and 93.3^{rd} percentiles of IMF11,IMF12's instantaneous period/frequency values, which roughly correspond to $\pm 1.5\sigma$(instantaneous periods). Fig. S1 (supplement) shows power spectra of IMF11 and IMF12, which visualise the range of periods the two modes have. Recall that instantaneous period/frequency can be obtained via Hilbert transform (see Eq. (B4) in Appendix B1). This range was chosen as it captures most of the variability in a given mode. Additionally, this range yields a good agreement with other methods (e.g., band-pass filtering), although other (reasonable) percentile ranges give qualitatively similar results. We then use these period/frequency ranges to perform a band-pass filter (via 5th order Butterworth filter) of the Niño3 index that is consistent with the individual modes (e.g., 29-53 months band of IMF12 is used to construct band-pass filtered Niño3 index composites in Fig. 6b; more below). We also use a band-pass filter of Niño3 index consistent with the sum of the two modes where the band-pass range encompasses periods of both significant modes, i.e., 16-53 months (e.g., used to construct black solid line in Fig. 3).

Timeseries of the sum of IMFs (black dashed line) and band passed index (black solid line) largely agree (i.e., their correlation is 0.95; Fig. 3). Also, the individual modes show very good agreement with the band-passed index with correlations of 0.68 (IMF11) and 0.83 (IMF12), which can be increased further if we consider only the specific IMF's timescale range (specified above) when band-passing the Niño3 index. This merely confirms that MEMD results are consistent with other filtering methods.

Additionally, timeseries of Niño3 index extracted from IMF11,12 (Fig. 3) are largely consistent with the modes identified in Jiang et al. (1995) (their Fig. 9a), who used MSSA analysis, and with Wang and Ren (2020) (their Fig. 3), who used EEMD on Niño3.4 index. IMF12 is also similar to Froyland et al. (2021) 4-year mode (their Fig. 10), who used an operator-theoretic approach. The average periods of the 'significant' modes of variability (IMF11,12) in this study are typically lower than in other
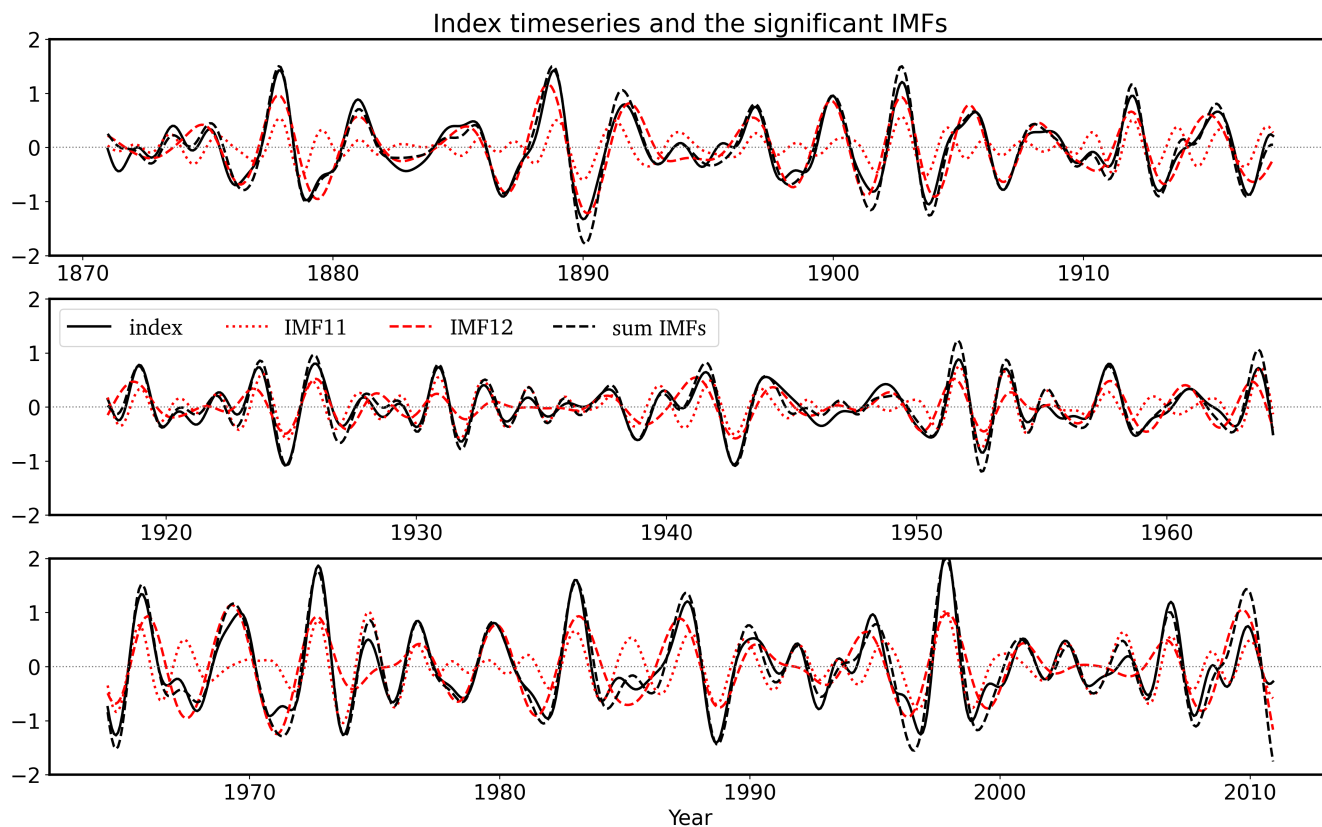
Figure 3. Timeseries (1871-2010) of Niño3 index from IMF11 (red dotted line) and IMF12 (red dashed line) obtained via MEMD. The sum of the two IMF indices (black dashed line) and band-pass filtered (16-53 months) Niño3 index (black solid line) are also shown. All data are standardised.

studies, however please recall that we have used much longer timeseries and that the timeseries of IMFs are nonstationary. Thus, within the overlapping time periods (e.g., recent decades), the timescale (and corresponding timeseries) is generally consistent across different studies. These similarities provide further confidence in the results from the MEMD. Note that these studies have focused on different ENSO timescales and associated different spatial patterns during QB and LF/QQ ENSO events. 305 However, IMFs are nonstationary and can thus capture changing patterns over time (section 5.3). Also, previous studies have not necessarily considered relationships between different variables that are relevant for the ENSO dynamics (section 6) and related conceptual oscillator models on specific timescales.

Overall, MEMD is consistent with other filtering methods (i.e., it acts like an effective band-pass filter) and can thus be used for further analysis of ENSO dynamics and its nonstationarity to determine if IMFs hold any physical significance. If 310 IMFs have physical meaning, the information inferred from them can be valuable for enhancing climate models, long-term

predictions, understanding teleconnections, and exploring the underlying physics and variability of specific fields of interest, such as ENSO. In the following sections we address some of these aspects.

5.3 Nonstationarity of ENSO

The period-ranges provided above (see also Fig. S1) suggest that there is some overlap between the period/frequency bands
315 of IMF11, IMF12, which is a result of nonlinear and nonstationary evolution of the modes (period is not constant as seen in Fig. 3). Indeed, there is a low (yet statistically significant) correlation between the two modes ($\sim$0.28). Thus, in some time-windows the two IMFs can describe the variability of a similar timescale (e.g., similar temporal evolution in Fig. 3 around years ~~1923-7~~1923-1927, 1951-1955, 1997), but in other time-windows they describe variability on different timescales. Despite changing periods, the two IMFs pass the red noise threshold in the Niño3 region and are therefore still considered significant
320 and thus *quasi*-periodic (sections 4, 5.1).

In some decades the band-pass-filtered Niño3 index (black solid line) is more consistent with the lower frequency IMF12 (red dashed line; approx. 1870-1917, 1968-2000) and in other periods with the higher frequency IMF11 (red dotted line; approx. 1917-1968, 2000-2010) (Fig. 3). This is consistent with the interdecadal shifts in the frequency of ENSO (Hu et al., 2017, 2020) that have occurred around years 1970 (from higher frequency to lower frequency) and 2000 (from lower frequency to higher
325 frequency). Similar behaviour can also be seen earlier in the record. We can also see interdecadal changes in the amplitude of the ENSO modes, i.e., middle panel (period 1920-1965) in Fig. 3 compared with top and bottom panels (periods 1870-1920, 1965-2010). This is somewhat consistent with Crespo et al. (2022), who found reduced amplitude of ENSO during 1901-1931 and 1935-1965 periods relative to post-1970 period.

Similarly, IMFs can capture different propagation directions of SST anomalies (Fig. 4). Previous studies have highlighted that
330 SST anomaly propagation changed from westward to stationary or eastward around 1970 (Fedorov and Philander, 2000, 2001; Wang and An, 2001). Indeed, the two IMFs show westward propagation of SST anomalies prior to 1970. However, after 1970 it is slightly more complex. SST anomaly propagation becomes stationary or eastward in IMF11 (except for a period just before 1990; Fig. 4a), but IMF12 (Fig. 4b) still indicates either stationary or westward propagation with some rare (eastward) exceptions. This is then reflected in the sum of the two modes (Fig. 4c), which generally shows variability in propagation of
335 SST anomalies post-1970. Furthermore, some of the characteristics of SST anomaly propagation from the sum of IMF11 and IMF12 carry over to 1-year low-passed SST anomalies (e.g., in the 1960s, 1980s; Fig. 4d).

ENSO events have also been characterised as east Pacific (EP) or central Pacific (CP) depending on the longitude where SST anomalies maximise (e.g., Kao and Yu, 2009; Singh and Delcroix, 2013; Zhang et al., 2019). The two IMFs are less able to reproduce this feature of ENSO diversity (Fig. 4). Most EP events are captured by IMF11,12. However, some CP events (e.g.,
340 early 1990s; Fig. 4d) are not captured by quasi-periodic modes of variability (Fig. 4a,b,c). This suggests that other processes are likely causing them, such as sub-ENSO variability (Keenlyside et al., 2007). Similarly, some persistent La Niña events (e.g., mid 1970s, mid-1980s and around year 2000; Fig. 4d) are not necessarily captured by the quasi-periodic modes of variability alone (potentially related to ENSO asymmetry; e.g., Choi et al. 2013; An et al. 2020). These results could also reflect that some aspects of ENSO nonlinearity are not represented by these two IMFs (e.g., Dommenget et al. 2013).
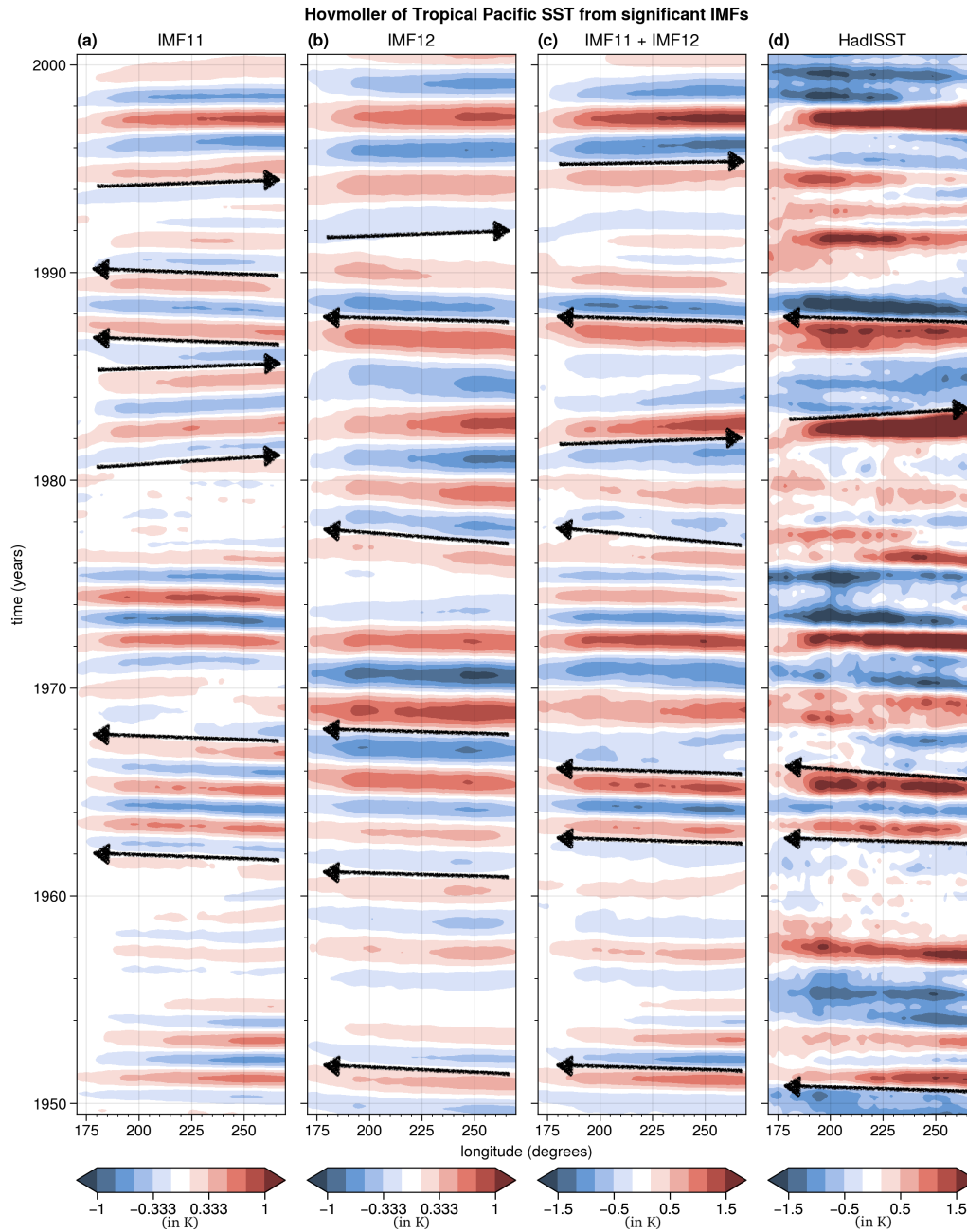
Figure 4. Time-longitude Hovmöller diagram of tropical Pacific SST anomalies (in K) averaged between 5°S and 5°N from (a) IMF11, (b) IMF12, (c) IMF11 + IMF12, and (d) 1-year low-passed (via 5th order Butterworth filter) SST data. Black arrows help visualise the direction of propagation of SST anomalies in some periods (other periods are more stationary). We show the time period around year 1970 (1950-2000) where a change in propagation direction has been identified in previous work. Note that colourscale in (a)-(b) is smaller than in (c)-(d).

345   Note that the magnitude of ENSO ultimately depends on all underlying modes of variability in the tropical Pacific (not just on the IMFs discussed here) — as also seen in Fig. 4. In fact, we find ∼5 modes (i.e., IMFs 10-14 here) with timescales ranging from ∼1 to ∼11 years (assessed via 6.7^{th} and 93.3^{rd} percentiles as above) that can reproduce the majority of ENSO variability (not shown), but the rest of these modes (i.e., IMF10,13,14 here) are consistent with red noise (Fig 2).

    Figs. 3, 4 also show that weak Niño3 events have either small amplitudes (e.g., 1930-40) of both IMFs or opposite amplitudes
350 (e.g., 1985-87). However, strong Niño3 events generally show a constructive interference or mode-combination (e.g., 1997, a super-El Niño event), which is consistent with, e.g., Slawinska and Giannakis (2017); Jajcay et al. (2018); Wang and Ren (2020); Froyland et al. (2021).

    This section has clearly demonstrated that MEMD together with a red noise test is suitable for identifying nonstationary quasi-periodic multivariate signals. This is a clear advantage of MEMD over other multivariate signal processing methods
355 (e.g., PCA, MSSA). Below we now turn to ENSO dynamics to show that IMFs are also physical.

6 ENSO dynamics

The dynamics of ENSO typically involves positive (e.g., Bjerknes) and negative feedbacks between the atmosphere and ocean. The Bjerknes feedback (Bjerknes, 1969) refers to any decrease (increase) of trade winds that leads to reduced (enhanced) ocean upwelling (downwelling) and thus warming (cooling) in the eastern tropical Pacific leading to reduced (enhanced) zonal SST-
360 and pressure-gradients, which in turn reinforce the initial increase (decrease) of the trade winds. The most prominent and also the simplest negative feedback in the tropical Pacific involves recharge/discharge of ocean heat content via Sverdrup transport (e.g., Jin, 1997a, b; Burgers et al., 2005). Other negative feedbacks involve propagation and reflection of ocean Rossby and Kelvin waves (e.g., Suarez and Schopf, 1988; Battisti and Hirst, 1989; Picaut et al., 1997; Weisberg and Wang, 1997; Wang et al., 1999; Wang, 2001, 2018), where the latter can also be wind-forced. These processes generally involve changes in the
365 thermocline depth, surface wind stress, and SST anomalies.

6.1 Quasi-oscillatory timescale

As ENSO dynamics is primarily related to the evolution of the ocean surface zonal wind stress (τ_x), thermocline depth and the SST in the tropical Pacific (e.g., Wang, 2018), we demonstrate their relationship with phase composite maps of IMF12 (Fig. 5). Shading in Fig. 5 represents SST anomalies, contours represent the thermocline depth anomalies (solid contours represent
370 positive values and deeper thermocline), yellow arrows represent τ_x anomalies, and grey shading represents grid points of the SST that do not pass the red noise threshold. All values are standardised (i.e., divided by standard deviation).

    The phase composites are computed using instantaneous phase of the IMF12's eastern Pacific SST (Niño3) timeseries (i.e., IMF12 (SST (Niño3))) that we can obtain via Hilbert Transform (Appendix B1, Eq. (B4)). This 'assigns' every point in the eastern Pacific SST (Niño3) timeseries a phase between 0 and 360 degrees, which can then be split into 12 phases (marked
375 phase 0 through 11; e.g., phase 0 is 0-30°, ..., phase 11 is 330-360°) and all points in timeseries (of 1-D or 3-D fields) belonging to a specific phase are then averaged to form map phase composites shown in Fig. 5 (see also Fig. S3 for IMF11). Line phase

composites in Fig. 6 (see also Fig. S4 for IMF11) are constructed similarly. Eastern Pacific SST (Niño3) is chosen as an index here to focus on East-Pacific (EP) ENSO events and related dynamics.

Fig. 5 shows a typical cycle of EP ENSO in the tropical Pacific (on a ∼3-year timescale) as composited over the IMF12's
380 Niño3 index. This cycle can also be summarised with line phase composites (Fig. 6a,c) by averaging over specific regions of the tropical Pacific (as labelled; see also Table 1). Here, we analyse eastern Pacific SST (Niño3), central Pacific τ_x (Niño4), western Pacific τ_x (Niño5), off-equatorial western Pacific thermocline depth (Niño6), and Pacific mean thermocline depth as they have historically been considered important for ENSO dynamics and have been used in ENSO conceptual oscillator models (e.g., Jin, 1997a; Burgers et al., 2005; Wang, 2018).

385 Together the two figures (Figs. 5, 6a,c) suggest the following sequence of events:

(i) during La Niña (phases 5-7) we have negative SST anomalies and shallower thermocline in Niño3 region, stronger easterly wind stress in Niño4 region, and deeper thermocline in the western Pacific (including Niño6 region);

(ii) as La Niña weakens (phases 8-10), the westerly wind stress in Niño5 region and thermocline depth averaged across the tropical Pacific peak, starting the El Niño cycle;

390 (iii) SST warm, eastern Pacific thermocline (Niño3) becomes deeper, central Pacific wind stress (Niño4) becomes westerly, and thermocline in the western Pacific (including Niño6 region) becomes shallower (phases 11,0,1);

(iv) El Niño weakens (phases 2-4) and western Pacific τ_x (Niño5) becomes easterly as well as the thermocline averaged across the Pacific becomes shallower, starting a La Niña event (phases 5-7);

(v) the cycle repeats.

395 The evolution described above is also seen in the band-pass (29-53 months; 2.5-4.5 years) filtered data (Fig. 6b). Note that the values in Fig. 6b are slightly larger than in Fig. 6a, because slightly different frequency ranges are ultimately represented in the two panels, but they remain qualitatively similar.

While Fig. 6 describes an average evolution of the variables considered, not all individual events have this exact behaviour. This is partly reflected in the reduced amplitudes of τ_x and thermocline depth in Fig. 6a compared with the SST amplitude. The
400 full timeseries of these parameters from IMF12 (Fig. 7; line types/colours are the same as in Fig. 6) show that the relationships from Fig. 6 occur often in the analysed period, especially for strong events. However, for weak events (middle panel in Fig. 7) the relationships are harder to establish — every event seems to be slightly different. This is somewhat consistent with Crespo et al. (2022), who noted that the dynamics of ENSO was different prior to 1970 relative to after 1970 with a dominant recharge-discharge oscillator (Jin, 1997a, b; Burgers et al., 2005) in the latter period.

405 Similar results (phase composites) can also be obtained for the 16-33 months band-passed data and IMF11 (Figs. S3, S4 in the supplement). This suggests that on average the QB and LF/QQ ENSO events have similar evolution and associated dynamics. However, the frequency of events (see full timeseries in Fig. S5 in the supplement) that follow the dynamics identified in the phase composites (Fig. S4) is lower in IMF11 case than in IMF12 case. This may be indicative of other processes that could be relevant for the QB ENSO.
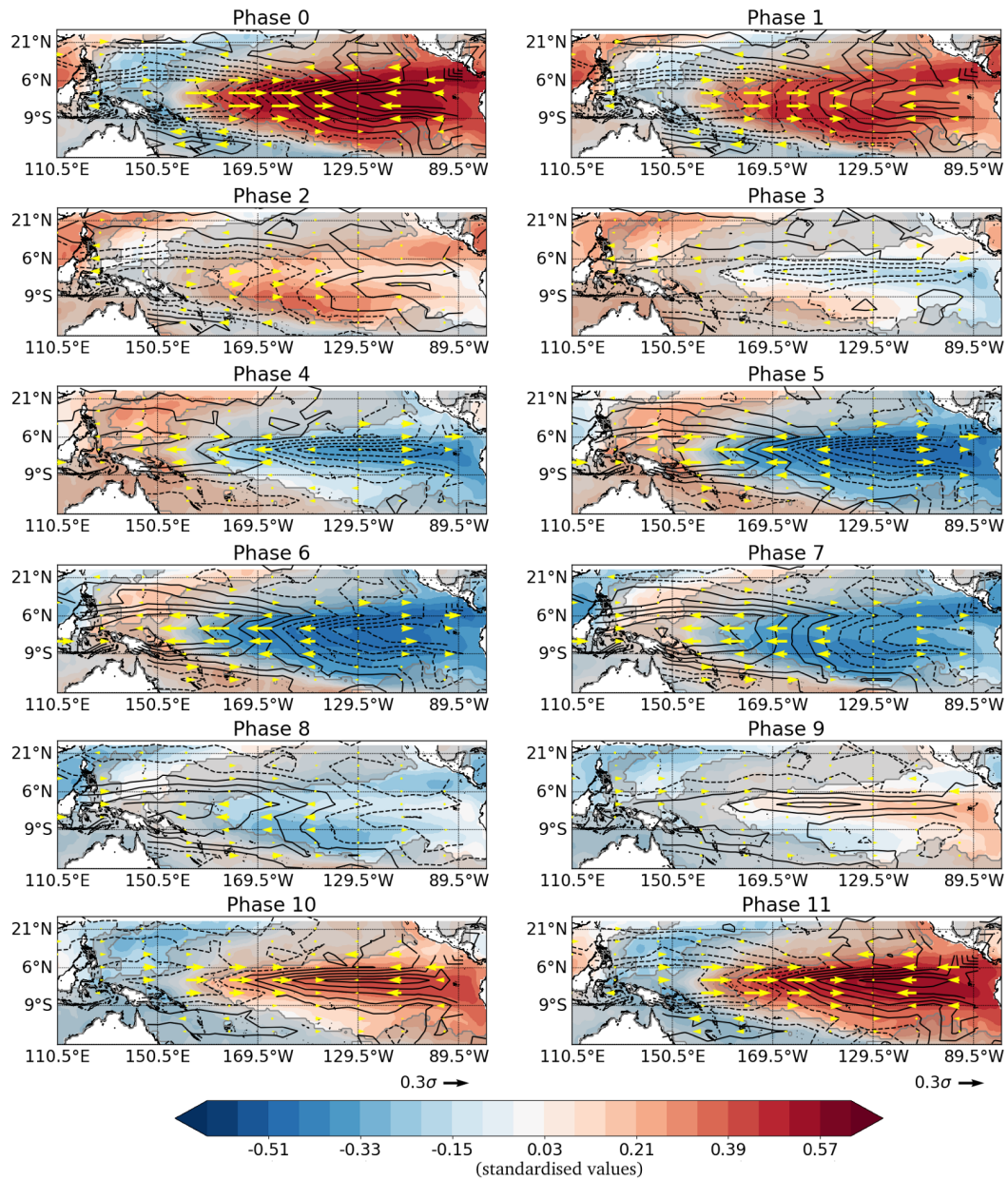
Figure 5. Latitude-longitude phase composite (phases 0 to 11 as labelled) of IMF12: shading for SST, contours for thermocline depth (contour interval is the same as in the colourbar with solid contours representing positive values, and dashed contours represent negative values), and arrows for τ_x (the scale is shown in the bottom left corner of panels for phases 10,11). All data is are standardised and all fields were composited based on the phase of the eastern Pacific SST (Niño3) index.
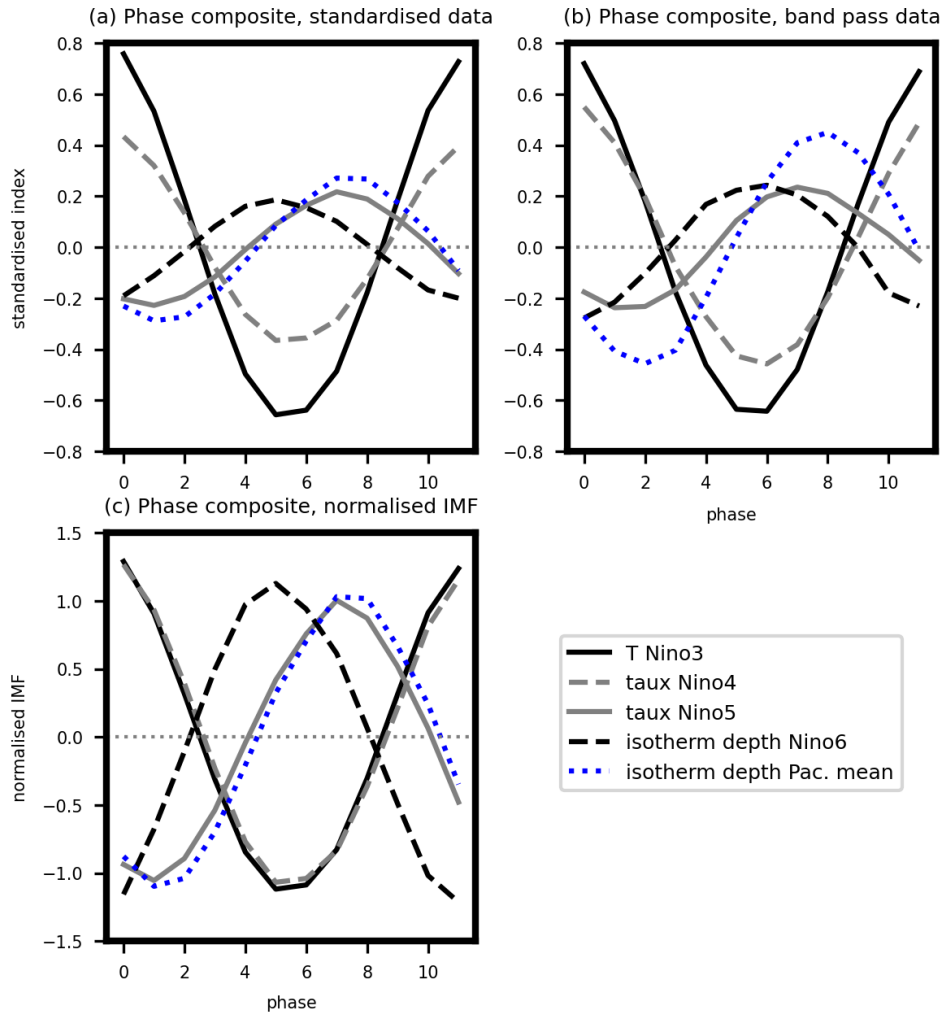
Figure 6. Phase composites of eastern Pacific SST (Niño3) (black solid line), off-equatorial western Pacific isotherm/thermocline depth (Niño6) (black dashed line), Pacific mean isotherm/thermocline depth (blue dotted line), central Pacific τ_x (Niño4) (grey dashed line), western Pacific τ_x (Niño5) (grey solid line). All fields are composited over the phases of eastern Pacific SST (Niño3), such that they fit the phases in Fig. 5. (a) composites of IMF12 for data divided by the standard deviation of corresponding timeseries (e.g., IMF12 (thermocline)/σ (thermocline)); (b) composites of band-pass filtered (29-53 months) standardised timeseries; (c) as in (a) but IMF-timeseries are divided by IMF's standard deviation (e.g., IMF12 (thermocline)/σ (IMF12 of thermocline)).

410   The results presented here and summarised in the line phase composites (Fig. 6, S4) have some interesting implications for the dynamics of ENSO and conceptual oscillator models. The out-of-phase relationship between Pacific mean thermocline depth (blue dotted line) and eastern Pacific SST (Niño3; black solid line) is a typical feature of the recharge-discharge oscillator (Jin, 1997a, b; Burgers et al., 2005). This suggests that IMFs that emerge from MEMD analysis can capture physical processes
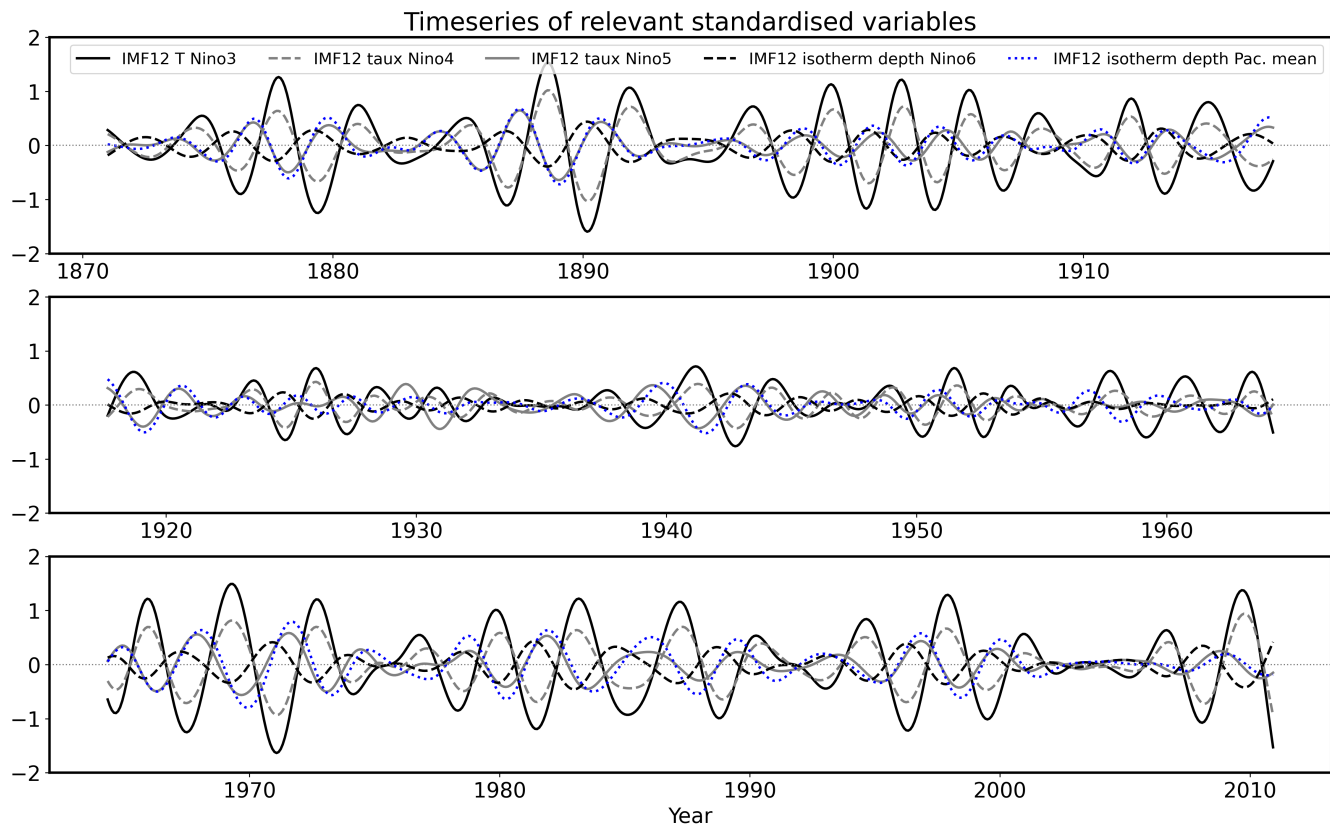
Figure 7. IMF12's standardised timeseries of eastern Pacific SST (Niño3) (black solid line), off-equatorial western Pacific thermocline depth (Niño6) (black dashed line), Pacific mean thermocline depth (blue dotted line), central Pacific τ_x (Niño4) (grey dashed line), western Pacific τ_x (Niño5) (grey solid line).

in the tropical Pacific. Furthermore, co-variability of the Pacific mean thermocline depth and the western Pacific wind stress (Niño5; grey solid line) suggests that wind forcing in the western Pacific may play a role in the recharge-discharge process or in the onset of ENSO in general as it precedes ENSO events (see also Roulston and Neelin, 2000; Capotondi et al., 2018; Lopez et al., 2013; Lopez and Kirtman, 2014; Timmermann et al., 2018).

On the other hand, the co-variability between central Pacific wind stress (Niño4; grey dashed line), off-equatorial western Pacific thermocline depth (Niño6; black dashed line) and eastern Pacific SST (Niño3; black solid line) suggests that the unified oscillator proposed by Wang (2001) may need to be revised (see also Graham et al., 2015). This is because: (i) in the unified oscillator model these three quantities should all be somewhat out-of-phase, but here we show that only western Pacific wind stress and Pacific mean thermocline depth exhibit out-of-phase relationship with eastern Pacific SST (on average); and (ii) Pacific mean thermocline depth does not co-vary with off-equatorial western Pacific thermocline depth (Niño6), rendering

the unified model's recharge-discharge oscillator simplification, which uses off-equatorial western Pacific thermocline depth
(Niño6), questionable.

That the central Pacific wind stress may be omitted in the *unified model* (due to co-variability with the eastern Pacific SST)
was also mentioned in Graham et al. (2015). However, they suggested that western Pacific wind stress (Niño5) could also
be omitted from the *unified model*, but Fig. 6 suggests that on 1.5-4.5 year timescale this variable should be kept. This may
be because Graham et al. (2015) used 1-year low-pass filtered data, which could have obscured the signal on 1.5-4.5 year
timescale (see section 6.2). Additionally, Graham et al. (2015) suggested using the thermocline depth in the western Pacific
averaged over a region that lies on the equator, rather than off-equator. From Fig. 5 we can see that this would likely yield
similar results as off-equatorial western Pacific thermocline depth (Niño6) (to ± 1 phase).

6.2 Other timescales

ENSO is a phenomenon that occurs on timescales of 2-8 years and previous work has often used 1-year low pass filter to obtain
ENSO. Thus, we now test the relationships between eastern Pacific SST (Niño3), central Pacific τ_x (Niño4), western Pacific
τ_x (Niño5), western Pacific off-equatorial thermocline depth (Niño6), and Pacific mean thermocline depth on slightly shorter
and slightly longer timescales. We do this to test how relationships between different variables change across timescales that
are still somewhat within the ENSO range.
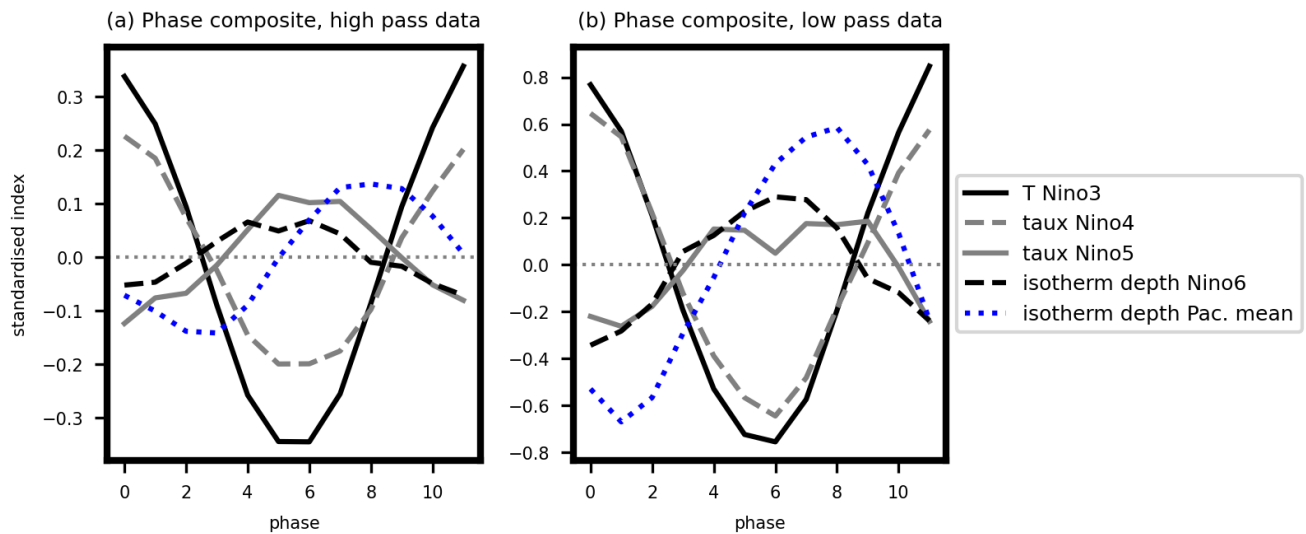
Figure 8. As in Fig. 6b, but for (a) higher frequency (band-pass filter over 12-19 months) data and (b) lower frequency (band-pass filter over 42-135 months) data. Note that higher and lower frequency timescale bands were chosen based on timescale ranges of 10th and 13th-14th IMFs, i.e., the IMFs with slightly smaller or larger (respectively) timescales than IMF11, IMF12.

Fig. 8 shows phase composites similar to those in Fig. 6b, but for band-passed data over 12-19 months range (shorter periods; Fig. 8a) and over 42-135 months range (longer periods; Fig. 8b). These timescale bands are consistent with IMF10 (shorter periods) and IMFs 13,14 (longer periods), which are the modes that together with IMF11,12 explain the majority of variance in, e.g., eastern Pacific SST (Niño3).

As in Fig. 6b, but for (a) higher frequency (band-pass filter over 12-19 months) data and (b) lower frequency (band-pass filter over 42-135 months) data. Note that higher and lower frequency timescale bands were chosen based on timescale ranges of 10th and 13th-14th IMFs, i.e., the IMFs with slightly smaller or larger (respectively) timescales than IMF11, IMF12.

Interestingly, on these shorter and longer timescales the evolution is different than on quasi-oscillatory timescales (1.5-4.5-year periods of IMF11,12). Namely, western Pacific wind stress (Niño5) closely follows western Pacific off-equatorial thermocline depth (Niño6) (Fig. 8a,b). This suggests a very different role of the western Pacific wind stress on different timescales, which may be relevant for ENSO diversity/asymmetry. However, other variables remain similar across timescales (to $\pm$ 1 phase). Thus, recharge-discharge processes operate throughout the ENSO timescale range (2-8 years), since Pacific mean thermocline depth and eastern Pacific SST (Niño3) remain out of phase also on these shorter/longer timescales. Also, the results from these shorter/longer timescales indicate that the western Pacific wind stress (Niño5) may be omitted from conceptual oscillator models (on these timescales) as it is anti-correlated with eastern Pacific SST (Niño3). This is consistent with Graham et al. (2015), who suggested this revision of the *unified oscillator*, but using 1-year low-pass filtered data, which may have obscured the different behaviour on quasi-periodic timescales (section 6.1; Fig. 6).

The above analysis shows that it is important to filter the data to "correct" frequency bands as there may be different behaviour present on different timescales, even within the ENSO range of 2-8 years.

7   Conclusions

In this study we have used a recently developed nonlinear and non-stationary method for identifying intrinsic variability of multivariate systems, the multivariate empirical mode decomposition (MEMD; Rehman and Mandic 2010). The method can objectively identify modes of variability on different timescales within a nonlinear and non-stationary dataset describing a complex system such as the climate system. The timescale identification is objective as it is done without any pre-selection of a timescale window in which we expect the quasi-periodic behaviour. It finds a signal that is synchronised across input timeseries (here PC timeseries of combined fields, i.e., SST, wind stress, thermocline depth over the tropical Pacific) for every timescale within the given system. Also, the multivariate modes of variability that emerge from MEMD analysis have non-stationary (i.e., evolving in time) patterns of variability (e.g., Fig. 4)—a clear advantage over some other multivariate timeseries analysis tools whose patterns are stationary.

Additionally, a red noise significance test has been developed to robustly identify quasi-periodic modes of variability in the given data, which had not been used before in the framework of MEMD. This means that MEMD can now be used as an alternative method for objective identification of the timescale of quasi-periodic motions in the climate system. Since the red

noise test can be applied on every grid point separately, MEMD together with the red noise test can also be used for identifying potential new regions of quasi-periodic variability (similar to Fig. 5).

We demonstrate that MEMD can identify physical quasi-periodic modes of variability within the climate system by analysing tropical Pacific SST variability. We have identified a clear quasi-periodic behaviour on a timescale of about 2-3 years (16-53 months) in the tropical Pacific. This timescale falls within the typical timescale range of ENSO, i.e., 2-8 years and the dynamics of this quasi-periodic variability is consistent with ENSO dynamics. While ENSO quasi-periodic variability is well-known, an identification (via MEMD) of a frequency range linked to the two dominant quasi-periodic modes of variability (i.e., 16-53 months) has still led to a few interesting results.

By analysing composites (e.g., Figs. 5, 6) of the thermocline depth, wind stress and SST, we have shown that the $\sim$2-3-year (~~Eastern~~ eastern Pacific) ENSO variability is generally consistent with the recharge-discharge conceptual oscillator model of ENSO (e.g., Jin, 1997a; Burgers et al., 2005). This oscillator describes an interplay between Pacific mean thermocline depth and eastern Pacific SST (Niño3), which are related to recharge and discharge of ocean heat content on a timescale of about 3 years. However, the unified model (Wang, 2001) may need to be revised (see also Graham et al., 2015) as most of the variables relevant for the unified oscillator model co-vary. In particular, western Pacific off-equatorial thermocline depth (Niño6), central Pacific wind stress (Niño4), and eastern Pacific SST (Niño3) exhibit the same phase relation and thus describe the same dynamics. As also western Pacific wind stress (Niño5; relevant for the unified oscillator) and Pacific mean thermocline depth co-vary, there seems to be a close relationship between the recharge-discharge and unified oscillator models, but it may be different than previously thought.

On shorter and longer timescales (12-19 months, 42-135 months; Fig. 8) the relationships between variables are different, specifically the western Pacific wind stress (Niño5) on these timescales co-varies with eastern Pacific SST (Niño3). This suggests that the role of the western Pacific atmosphere-ocean processes (via wind stress) in tropical Pacific variability (and ENSO) can be very different on different timescales, whereas other variables (and in other regions) largely keep their relationships across timescales. This means that recharge-discharge oscillator model operates on all timescales considered (12-135 months), even if it has a characteristic timescale. However, the relations underlying the unified oscillator model exhibit different behaviour on different timescales, implications of which should be explored further in the future.

MEMD analysis could be extended in several ways. For example: (i) to assess ENSO dynamics in models as they typically struggle with the representation of the western Pacific processes (i.e., relevant for Niño5 wind stress; Guilyardi et al., 2020; Planton et al., 2021); and (ii) to study ENSO teleconnections on different timescales (e.g., Brönnimann, 2007; Fereday et al., 2008; Jiménez-Esteve and Domeisen, 2018; Jiménez-Esteve and Domeisen, 2020; Hardiman et al., 2019). Also, future studies should involve an examination of sensitivity and causal links (not established here) between different variables and their links across scales (e.g., Runge et al., 2015; Jajcay et al., 2018; Jenney et al., 2019; Kretschmer et al., 2021), as well as dedicated model-experiments.

Overall, this study has analysed the variability in the tropical Pacific (using MEMD with a red noise test), identified two quasi-periodic modes of variability (on $\sim$2-3-year timescale), related their physics to the recharge-discharge oscillator, and suggested a revision to the unified oscillator model (somewhat consistent with Graham et al., 2015). As the variability on this

timescale is quasi-periodic, it may be predictable far in advance, which calls for further investigations of the tropical Pacific variability and related teleconnections, their prediction, and for further model improvements (see also Chen et al., 2021; Lee et al., 2021).

Code availability. EMD and MEMD Python codes are available on Github (https://github.com/laszukdawid/PyEMD,
510 https://github.com/mariogrune/MEMD-Python-). Other scripts are available upon request.

Data availability. SODA2 data can be downloaded from http://apdrc.soest.hawaii.edu/dods/public_data/SODA/soda_pop2.2.4;
HadISST data can be downloaded from https://www.metoffice.gov.uk/hadobs/hadisst.

Appendix A: MEMD for 3-D fields

To find the intrinsic variability of our 3-D field, i.e., $\mathbf{A}'(L_t, L_y, L_x)$ mentioned in section 3.3, we first reduce dimensionality of
515 our data by decomposing it using the singular value decomposition (SVD), which yields spatial patterns of our data (empirical orthogonal functions, EOFs) and corresponding timeseries (principal components, PCs). First, we multiply $\mathbf{A}'$ by $\sqrt{\cos\phi}$ (area weighting; with ϕ latitude), divide by standard deviation (σ) at each grid point (and for each variable separately, if relevant), and reshape $\mathbf{A}'$ from 3-D array (L_t, L_y, L_x) to 2-D array $(L_t, L_x \cdot L_y)$. Then $\mathbf{A}'$ can be expressed with a singular value decomposition as

$$520 \quad \sigma^{-1}(L_x \cdot L_y)\mathbf{A}'(L_t, L_x \cdot L_y) = \mathbf{U\Sigma V}^T \tag{A1}$$

where $\mathbf{U}$ and $\mathbf{V}$ represent left and right singular vectors related to PCs and EOFs, $\mathbf{\Sigma} = \sqrt{(L_t - 1)\mathbf{\Lambda}}$ is a diagonal matrix with square roots of variance explained of each mode (denoted $\mathbf{\Lambda}$, i.e., eigenvalues) along the diagonal, L_t is the length of timeseries, and superscript T denotes transpose. PCs are defined as $\mathbf{U}\sqrt{L_t - 1}$ and EOFs as $\mathbf{\Sigma V}^T/\sqrt{L_t - 1}$, such that $\sigma^{-1}(L_x \cdot L_y)\mathbf{A}'$ can be represented as a function of PCs and EOFs

$$525 \quad \sigma^{-1}(L_x \cdot L_y)\mathbf{A}'(L_t, L_x \cdot L_y) \simeq \sum_{m=1}^{m=20} \mathrm{EOF}(m, L_x \cdot L_y)\mathrm{PC}(m, L_t) \tag{A2}$$

where m corresponds to PC-number and is ordered according to the eigenvalues ($m = 1$ for the largest eigenvalue). We retain only the leading 20 PCs for the analysis (they generally describe the majority of the variance in $\mathbf{A}'$).

Now we can use the 20 PCs ($\mathrm{PC}(m, L_t)$) as input to MEMD algorithm (for details on algorithm itself see Rehman and Mandic 2010). This algorithm finds common timescales (i.e., Intrinsic Mode Functions, IMFs) within the 20 PCs and splits
530 each PC into several IMFs (the number of IMFs is not predetermined). Thus, each PC can be represented as a sum of IMFs

$$\mathrm{PC}(m, L_t) = \sum_{s=1}^{s=s_{max}} \mathrm{IMF}(s, m, L_t) \tag{A3}$$

where s corresponds to IMF-number and is ordered according to the timescale ($s = 1$ for the shortest timescale, s_{max} for the longest timescale, which is usually a trend or a residual). Eq. (A3) shows that each PC is a superposition of different IMFs (see also Table S2) and with it also a superposition of modes of variability in the selected field(s) with different timescales.

Each PC is associated with a spatial pattern ($\text{EOF}(m, L_x \cdot L_y)$), which allows a reconstruction of the time-space $(L_t, L_x \cdot L_y)$ structure/evolution for each IMF, yielding IMFs of initial dataset $\mathbf{A}'$ (**IMFA**). We do this by multiplying PCs for each IMF with corresponding EOFs and summing over all 20 PCs/EOFs (similar to Eq. A2)

$$\sigma^{-1}(L_x \cdot L_y)\mathbf{IMFA}(s, L_t, L_x \cdot L_y) \simeq \sum_{m=1}^{m=20} \text{IMF}(s, m, L_t)\text{EOF}(m, L_x \cdot L_y). \tag{A4}$$

Here note that to get **IMFA** in the units of the input field we must multiply it by the field's standard deviation as the input data for the SVD algorithm were standardised (Eq. A1). Again, **IMFA**s are ordered by timescale, i.e., **IMFA**1 with the shortest timescale and **IMFA**s_{max} with the longest timescale (trend). From here we can reconstruct $\mathbf{A}'$ by summing over all **IMFA**

$$\sigma^{-1}(L_x \cdot L_y)\mathbf{A}'(L_t, L_x \cdot L_y) \simeq \sum_{s=1}^{s=s_{max}} \mathbf{IMFA}(s, L_t, L_x \cdot L_y) \tag{A5}$$

and ultimately one can also reshape $\mathbf{A}'$ from 2-D array $(L_t, L_x \cdot L_y)$ to 3-D array (L_t, L_x, L_y). The importance of each **IMFA** for $\mathbf{A}'$ can be assessed by computing variance explained of each **IMFA** or other significance methods. To find **IMFA** modes (and grid-points) that correspond to potentially oscillatory behaviour we must perform a red noise test (see Appendix B).

Note that from here on (and in the main text) **IMFA**s are referred to as IMFs for simplicity.

Appendix B: Significance tests

Typically we can test if the modes (IMFs) are different from white or red noise, depending on the distribution of our data. In the climate system, variables often exhibit behaviour that resembles white or red noise. The IMFs that are significant (i.e., different from both red and white noise) likely represent quasi-oscillations, indicating higher potential for predictability of processes that correspond to the timescale of the significant IMF. Thus, this distinction is very important in climate science. Therefore, we discuss the white and red noise tests (for 1-D data, i.e., timeseries) below, whereas the robustness of IMFs from MEMD analysis and the relevant significance tests are discussed in the main text (sections 4, 5).

Note that the white and red noise tests are performed on 1-D timeseries, hence EMD (univariate decomposition; see main text) is first used to test the performance of IMFs that arise from the EMD analysis. The multivariate data (via MEMD) in the main text is analysed with the simplest and most relevant test (i.e., theoretical red noise test described below).

B1   White noise test

The white noise significance test has been derived by Wu and Huang (2004), who showed that the energy density function of sth IMF (E_s; i.e., average squared amplitude of the sth IMF) is

$$E_s = \frac{1}{L_t}\sum_{j=1}^{L_t}[\text{IMF}_s(j)]^2, \tag{B1}$$

where $\text{IMF}_s(j)$ is the sth IMF at time-step j ($j = 1, ..., L_t$), and L_t is the length of the timeseries. Wu and Huang (2004) further showed that the total energy density of the sth IMF can then be expressed as

$$L_t E_s = \int S(\nu)_s \mathrm{d}\nu \tag{B2}$$

where ν is frequency, and $S(\nu)_s$ is the power spectrum of the sth IMF. From this they showed that for white noise

$$\ln E_s \approx -\ln T_s \tag{B3}$$

where T_s is the average period of the sth IMF, and $\ln$ denotes natural logarithm.

Note that frequency (and thus also period) of each IMF is computed using Hilbert transform by first generating an analytical signal (e.g., Huang et al., 1998)

$$Z(t) = X(t) + \mathrm{i}Y(t) = |Z(t)|\mathrm{e}^{\mathrm{i}\theta(t)} \tag{B4}$$

where t is time dimension, $X(t)$ is our IMF timeseries, $Y(t)$ is its Hilbert transform, $Z(t)$ is the analytical signal, and $\theta(t) = \arctan(Y(t)/X(t))$ is instantaneous phase. Instantaneous frequency can then be computed by taking a time-derivative of the phase, i.e., $\nu = \mathrm{d}\theta(t)/\mathrm{d}t/2\pi$, and the average frequency of each IMF is computed by averaging instantaneous frequency in time (note that period = $1/\nu$, i.e., T_s).

The relationship between the logarithms of energy density and average period of the IMFs (Eq. B3) is then used in Fig. B1a (black solid line) to test whether an IMF (using EMD decomposition of Niño3 index; blue dots in Fig. B1a; see also section 3) is different from white noise or not. The mode is significant with respect to white noise if it exceeds one-tailed 95th percentile threshold (denoted by black dotted line). The percentile range serves as a significance test, i.e., if IMFs from our data are above, e.g., 95th percentile they are significant at 95th percentile level. The percentile range can be expressed analytically as (Wu and Huang, 2004)

$$\ln E_s = -\ln T_s \pm p\sqrt{\frac{2}{L_t}} \exp(\ln T_s/2) \tag{B5}$$

where p denotes a threshold ($p = 1.645$ for one-tailed 95th percentile of Gaussian distribution). Note that typically the number of degrees of freedom (DoF) for white noise data is expected to be equal to the total energy density of the sth IMF (i.e., $\text{DoF}_s = L_t E_s$; Wu and Huang 2004).

Alternatively, we can test whether the input data is different from white noise by constructing multiple (I) realisations of synthetic white noise timeseries w_i (i^{th} random normally distributed timeseries with standard deviation σ of 1). Then we can compute its IMFs via EMD (section 3) and we can repeat the process I-times. Employing Eq. B1 on these IMFs yields scattered grey dots in Fig. B1a (constructed in the same way as blue dots; see also section 4, Fig. 2), where their mean and 5th-95th percentile are shown as grey solid and dotted lines, respectively.

A comparison with the IMFs from the input data (Niño3 index; blue dots in Fig. B1a) reveals that many IMFs lie outside the white noise range and that overall the data (blue dots) distribution does not resemble the white noise (grey dots) distribution
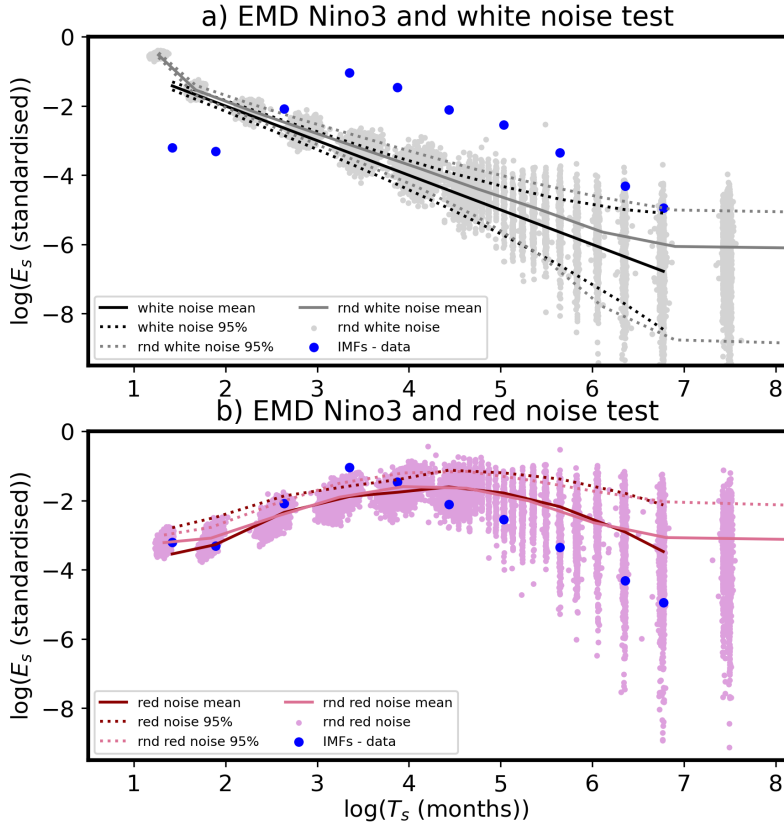
Figure B1. Significance tests for EMD modes: (a) white noise significance test and (b) red noise significance test for EMD-IMFs of Niño3 index (blue dots). Blue dots are computed as in Fig. 2. (a) Black solid line represents the theoretical linear relationship between the logarithms of period (T_s) and logarithm of energy density (E_s; i.e., average squared amplitude; Eq. (B3)), black dotted line represents 5th-95th percentile (Eq. B5), respectively; grey dots represent $I = L_t$ realisations of IMFs of white noise timeseries (length is the same as for Niño3 index), whereas grey solid and dotted lines represent their mean and the 5th-95th percentile, respectively. (b) Red solid line represents the theoretical red spectrum energy density (Eqs. (B7-B9)), red dotted line represents the 95th percentile (via χ^2-test); light pink dots represent $I = L_t$ realisations of IMFs of red noise timeseries (Eq. B6; length L_t is the same as for Niño3 index), whereas pink solid and dotted lines represent their mean and the 95th percentile, respectively. Note that x-axis shows the logarithms of period ($\log_e(T_s)$) ordered from shortest period (highest frequency) to longest period (trend). For further descriptions of the figure see text.

(not noted in Wu and Huang 2004). This suggests that a white noise test for such data is not a good test. Indeed, atmosphere-ocean coupled systems, such as ENSO, can often be represented as a red noise process (e.g., Hasselmann 1976; Frankignoul and Hasselmann 1977), thus we now turn to a similar test, but for data distributed as red noise.

B2 Red noise test

B2.1 Synthetic red noise data

To test if our data (e.g., Niño3 index) is purely red noise or it has inherent oscillations that we can identify through the (M)EMD analysis, we generate I-realisations of synthetic red noise timeseries x (AR(1) process) as (e.g., Gilman et al. 1963)

$$x_{i,j+1} = r x_{i,j} + \sqrt{1 - r^2}\, w_{i,j+1} \tag{B6}$$

where r is lag-1 auto-correlation from our data (e.g., Niño3 index), w is white noise (as in Appendix B1), i runs over I realisations of synthetic red noise data, and j ($j > 1$ and $j \leq L_t$; with L_t length of our data, e.g., the length of Niño3 record) is an index that runs over the time-steps (one time step is one time unit, e.g., 1 month). For $j = 1$ (the first time-step) we set $x_{i,1} = w_{i,1}$.

Once we obtain the red noise timeseries x_i we can compute its IMFs via EMD (section 3) and we can repeat the process I-times (as for the white noise; Appendix B1). This yields the pink scattered dots in Fig. B1b. The mean over I cases for each IMF (frequency band) is shown by pink solid line and the (one-tailed) 95th percentile across the I cases are shown by pink dotted line. Note that we plot logarithmic values in Fig. B1, as mentioned above.

Note that Franzke (2009) used a similar approach for indices such as the North Atlantic Oscillation, and found a simple relationship between the power spectrum and frequency, consistent with Kolotkov, D. Y. et al. (2016). However, we follow Gilman et al. (1963) to define a relationship between the power spectrum and frequency. This incorporates the lag-1 auto-correlation of the timeseries into the theoretical red noise power spectrum (see below).

B2.2 Theoretical red noise test

Alternatively, one can compute a theoretical power spectrum of the red noise (cf., Gilman et al. 1963)

$$S(\nu) = \frac{1 - r^2}{1 - 2r \cos 2\pi\nu + r^2} \tag{B7}$$

where S is the power spectrum of red noise, $\nu = 1/t$ is frequency, and r is again lag-1 auto-correlation from our data. For each frequency estimate we must multiply $S(\nu)$ by frequency range ($\Delta\nu$) (cf. Eq. (B2)) to obtain a theoretical estimate of the (mean) energy of the red noise (E^{red}) (cf. Kolotkov, D. Y. et al. 2016)

$$E^{red}(\nu) = S(\nu)(\nu\alpha - \nu/\beta) \tag{B8}$$

where $\beta = \sqrt{\nu_s/\nu_{s+1}}$ and $\alpha = \sqrt{\nu_{s-1}/\nu_s}$ with s running over frequencies (from higher to lower frequency). Note that since EMD is a dyadic filter (each lower frequency is a half of the previous one; e.g., Flandrin et al. 2004; Rehman and Mandic 2011) both α and β typically take a value of $\sqrt{2}$ (consistent with, e.g., Kolotkov, D. Y. et al. 2016). However, when mode-mixing is present (e.g., here it is generally present at higher and lower frequencies of IMFs from MEMD analysis) this is not necessarily true, hence the use of α and β in Eq. (B8). Finally, E^{red} for every s^{th} IMF (i.e., E_s^{red}) must be scaled such that its total energy
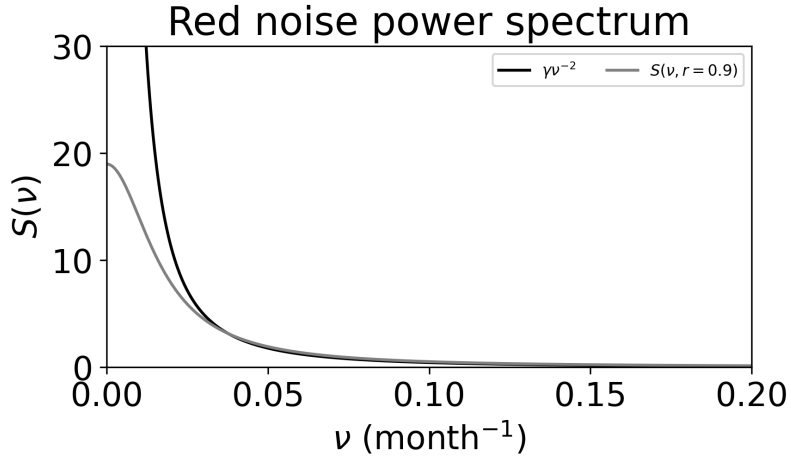
Figure B2. Red noise power spectrum ($S(\nu)$) for (black line) $S(\nu) = \gamma\nu^{-2}$, and (grey line) $S(\nu, r)$ from Eq. (B7) for $r = 0.9$. γ was estimated as a ratio between the integrated power spectra of the two spectra for frequencies higher than 0.02/month ($\gamma = \sum_\nu \nu^{-2} / \sum_\nu S(\nu, r)$) where the two power spectra generally agree well.

is the same as the total energy of our data (e.g., Madden and Julian 1971; Bretherton et al. 1999)

$$E_s^{red} = E_s^{red} \frac{\sum_{s=2}^{s_{max}-1} E_s}{\sum_{s=2}^{s_{max}-1} E_s^{red}} \tag{B9}$$

625   where s_{max} is the number of IMFs (as above), and s represents the sth IMF of frequency ν_s, and E_s was defined above (Eq. (B1)). Note that we scale E_s^{red} from total energies of IMFs between $s = 2$ and $s = s_{max} - 1$ as the last IMF is typically a trend/residual and the first IMF does not necessarily follow the distribution correctly (but including the two usually does not significantly alter the results). E_s^{red} is shown in Fig. B1b as red solid line.

    This red noise test is typically used in climate science to determine the significance of power spectra peaks in our data
630   (using $S(\nu)$ from Eq. (B7)), and it differs from the red noise test of Kolotkov, D. Y. et al. (2016) as it takes into consideration the lag-1 auto-correlation of the data. If the cosine function in the $S(\nu)$ (Eq. (B7)) is expanded into Taylor series ($\cos 2\pi\nu \approx 1 - (2\pi\nu)^2/2 + ..$) one can realise that for large ν (high frequencies) $S(\nu)$ indeed reduces to the spectrum $\gamma\nu^{-2}$ (with γ a constant) suggested by Kolotkov, D. Y. et al. (2016); Franzke (2009). However, for low frequencies (small ν) they do not agree well and ultimately $S(\nu)$ also becomes a constant (see Fig. B2 for comparison). Furthermore, as $S(\nu)$ depends on lag-1
635   auto-correlation (r) we can see from Eq. (B7) that for $r = 0$, $S(\nu) = 1$, i.e., it reduces to the power spectrum of the white noise. This means that this theoretical test can potentially be used for testing the significance of the data that corresponds to either white or red noise.

    The significance of the IMFs from the input data is tested using χ^2-test, where s^{th} IMF's χ_s^2 value for the (one-tailed) 95th percentile is computed from $\mathrm{DoF}_s = L_{eff}E_s$ degrees of freedom (instead of $L_t E_s$ as was the case for white noise, due
640   to strong correlations between neighbouring data-points; Bretherton et al. 1999; Wu and Huang 2004; Kolotkov, D. Y. et al.

2016), where

$$L_{eff} = \frac{1-r^2}{1+r^2} L_t. \tag{B10}$$

Then we multiply the expected red noise curve E_s^{red} by χ_s^2/DoF_s (e.g., Madden and Julian 1971; Bretherton et al. 1999) to ultimately obtain a threshold for 95th percentile (red dotted line in Fig. B1b). Note that for $\text{DoF}_s < 1$ we set $\text{DoF}_s = 1$ (to

645   avoid numerical issues). The IMFs derived from the data (blue dots in Fig. B1b) that exceed the red noise threshold (i.e., lie above the red/pink dotted line in Fig. B1b) are considered significant at 95th percentile (one-tailed).

Fig. B1b shows that the two (synthetic and theoretical) red noise tests (for Niño3 index via EMD) are somewhat comparable and that the majority of the input (e.g., Niño3 index) data (blue dots) lies within the red noise range (i.e., within the pink-dots, and below the pink/red dotted line). However, we can identify one IMF (period ∼31 months or ∼2.5 years) that is above the

650   red noise threshold and well within the typical ENSO timescale (2-8 years), suggesting quasi-periodic behaviour (oscillations).

Similarly, we can use the theoretical red noise significance test on IMFs obtained via MEMD, which yields 2 significant modes of variability in the eastern Pacific SST (Niño3) index (see the main text). Note, however, that we do not necessarily expect exactly the same results from EMD (Fig. B1b) and MEMD (Fig. 2) methods since the MEMD finds a "synchronised" signal within the tropical Pacific and across different variables, whereas EMD only analyses the 1-D Niño3 timeseries. This is

655   also true for the number of IMFs obtained via the two different methods. MEMD yields significantly more IMFs as EMD (21 versus 10), which is likely a result of inputting several different timeseries with different timescales, especially in the high- and low-frequency range (i.e., periods shorter than about 8 months and longer than about 700 months).

Alternatively, one can also compute significant modes by computing red noise test at each grid-point and then average the results over all grid-points, but we have not used this here. Instead, we use an additional test on map-plots in section 5 (Fig.

660   5; Fig. S3 in supplement), where we identify *potentially* "oscillatory" grid points and use grey shading on areas that are well represented with red noise alone (i.e., not significant).

Despite some differences between the MEMD and EMD modes of variability (primarily due to different input timeseries), the two methods agree on the quasi-periodic timescale of 2-3 years in the Niño3 region. This is also consistent with the significant periods inferred from the usual 1-D wavelet transform (not shown) and the power spectrum analysis of the Niño3

665   index (1-D) obtained via Fourier Transform (Fig. B3). The latter confirms that 2-3 year timescale is quasi-periodic as there is a significant peak in the power spectrum of the Niño3 index on those timescales, i.e., black solid line in Fig. B3 (Niño3 index) is above the red dashed line (red noise one-tailed 95% threshold).
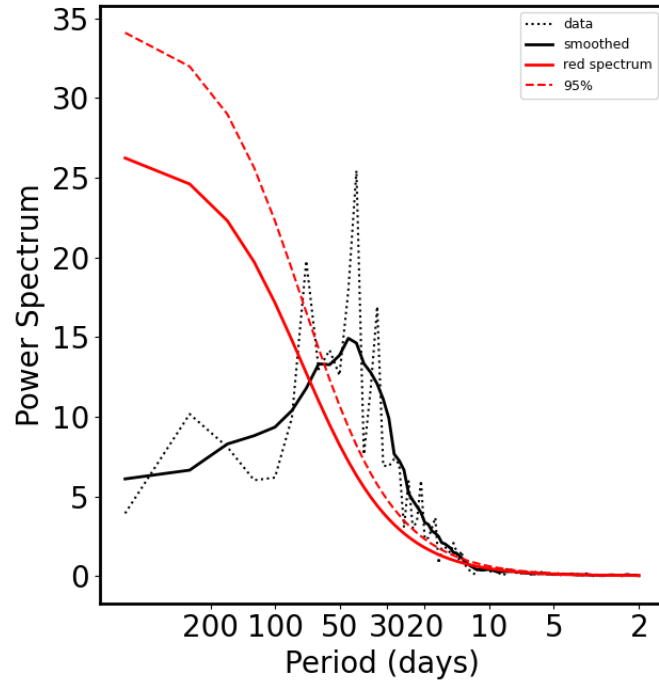
Figure B3. Power spectrum of Niño3 index. The power spectra are first computed for 500-months long chunks (overlapped by 250 months) and then averaged over all cases (grey solid line). The black solid line represents a 10-point running mean of the black dotted line (to increase the number of degrees of freedom, which is $f_\omega L_t / 0.5 L_{\mathrm{chunk}} = 10 \times 1680/250 \approx 67$; see also Boljka et al. 2021). The red solid and dashed lines represent the theoretical red noise test and its (one-tailed) 95th percentile, respectively.

Author contributions. LB performed the analysis, prepared the figures, and wrote the first draft of the manuscript. NEO and NSK provided additional insight and helped improve the manuscript for the final version.

670   *Competing interests.* The authors declare no competing interests.

Acknowledgements. This work was supported by the Trond Mohn Foundation (project BCPU, grant number BFS3018TMT01) and was performed on NIRD/Sigma2 (project NS9039K). We thank three anonymous reviewers and William Roberts for their constructive comments that helped improve the original manuscript. We also thank Lander Crespo for helpful discussions, and Ingo Bethke for ~~the~~ help with the data.

References

Alberti, T., Donner, R. V., and Vannitsem, S.: Multiscale fractal dimension analysis of a reduced order model of coupled ocean–atmosphere dynamics, Earth System Dynamics, 12, 837–855, https://doi.org/10.5194/esd-12-837-2021, 2021.

Allan, R. J.: ENSO and Climatic Variability in the Past 150 Years, p. 3–56, Cambridge University Press, https://doi.org/10.1017/CBO9780511573125.002, 2000.

An, S.-I., Tziperman, E., Okumura, Y. M., and Li, T.: ENSO Irregularity and Asymmetry, chap. 7, pp. 153–172, American Geophysical Union (AGU), https://doi.org/https://doi.org/10.1002/9781119548164.ch7, 2020.

Ashok, K., Behera, S. K., Rao, S. A., Weng, H., and Yamagata, T.: El Niño Modoki and its possible teleconnection, Journal of Geophysical Research: Oceans, 112, https://doi.org/https://doi.org/10.1029/2006JC003798, 2007.

Baede, A., Ahlonsou, E., Ding, Y., and Schimel, D.: The Climate System: an Overview, pp. 1–881, Cambridge University Press, Cambridge, United Kingdom and New York, NY, USA, https://www.ipcc.ch/report/ar3/wg1/chapter-1-the-climate-system-an-overview/, 2001.

Battisti, D. S. and Hirst, A. C.: Interannual Variability in a Tropical Atmosphere–Ocean Model: Influence of the Basic State, Ocean Geometry and Nonlinearity, Journal of Atmospheric Sciences, 46, 1687 – 1712, https://doi.org/10.1175/1520-0469(1989)046<1687:IVIATA>2.0.CO;2, 1989.

Bejarano, L. and Jin, F.-F.: Coexistence of Equatorial Coupled Modes of ENSO, Journal of Climate, 21, 3051 – 3067, https://doi.org/10.1175/2007JCLI1679.1, 2008.

Bjerknes, J.: ATMOSPHERIC TELECONNECTIONS FROM THE EQUATORIAL PACIFIC, Monthly Weather Review, 97, 163 – 172, https://doi.org/10.1175/1520-0493(1969)097<0163:ATFTEP>2.3.CO;2, 1969.

Boljka, L., Thompson, D. W. J., and Li, Y.: Downstream Suppression of Baroclinic Waves, Journal of Climate, 34, 919 – 930, https://doi.org/10.1175/JCLI-D-20-0483.1, 2021.

Bretherton, C. S., Widmann, M., Dymnikov, V. P., Wallace, J. M., and Bladé, I.: The Effective Number of Spatial Degrees of Freedom of a Time-Varying Field, Journal of Climate, 12, 1990 – 2009, https://doi.org/10.1175/1520-0442(1999)012<1990:TENOSD>2.0.CO;2, 1999.

Broomhead, D. S., Jones, R., and King, G. P.: Topological dimension and local coordinates from time series data, Journal of Physics A: Mathematical and General, 20, L563–L569, https://doi.org/10.1088/0305-4470/20/9/003, 1987.

Brönnimann, S.: Impact of El Niño–Southern Oscillation on European climate, Reviews of Geophysics, 45, https://doi.org/https://doi.org/10.1029/2006RG000199, 2007.

Burgers, G., Jin, F.-F., and van Oldenborgh, G. J.: The simplest ENSO recharge oscillator, Geophysical Research Letters, 32, L13 706, https://doi.org/https://doi.org/10.1029/2005GL022951, 2005.

Capotondi, A., Sardeshmukh, P. D., and Ricciardulli, L.: The Nature of the Stochastic Wind Forcing of ENSO, Journal of Climate, 31, 8081 – 8099, https://doi.org/10.1175/JCLI-D-17-0842.1, 2018.

Carton, J. A. and Giese, B. S.: A Reanalysis of Ocean Climate Using Simple Ocean Data Assimilation (SODA), Monthly Weather Review, 136, 2999 – 3017, https://doi.org/10.1175/2007MWR1978.1, 2008.

Chen, H.-C., Jin, F.-F., Zhao, S., Wittenberg, A. T., and Xie, S.: ENSO Dynamics in the E3SM-1-0, CESM2, and GFDL-CM4 Climate Models, Journal of Climate, pp. 1 – 59, https://doi.org/10.1175/JCLI-D-21-0355.1, 2021.

Choi, K.-Y., Vecchi, G. A., and Wittenberg, A. T.: ENSO Transition, Duration, and Amplitude Asymmetries: Role of the Nonlinear Wind Stress Coupling in a Conceptual Model, Journal of Climate, 26, 9462 – 9476, https://doi.org/https://doi.org/10.1175/JCLI-D-13-00045.1, 2013.

Crespo, L. R., Rodríguez-Fonseca, M. B., Polo, I., Keenlyside, N., and Dommenget, D.: Multidecadal variability of ENSO in a recharge oscillator framework, Environmental Research Letters, 17, 074 008, https://doi.org/10.1088/1748-9326/ac72a3, 2022.

de la Cámara, A., Birner, T., and Albers, J. R.: Are Sudden Stratospheric Warmings Preceded by Anomalous Tropospheric Wave Activity?, Journal of Climate, 32, 7173–7189, https://doi.org/10.1175/JCLI-D-19-0269.1, 2019.

Dommenget, D., Bayr, T., and Frauen, C.: Analysis of the non-linearity in the pattern and time evolution of El Niño southern oscillation, Climate Dynamics, 40, 2825–2847, https://doi.org/10.1007/s00382-012-1475-0, 2013.

Duffy, D. G.: The Application of Hilbert–Huang Transforms to Meteorological Datasets, Journal of Atmospheric and Oceanic Technology, 21, 599 – 611, https://doi.org/10.1175/1520-0426(2004)021<0599:TAOHTT>2.0.CO;2, 2004.

Ezer, T. and Corlett, W. B.: Is sea level rise accelerating in the Chesapeake Bay? A demonstration of a novel new approach for analyzing sea level data, Geophysical Research Letters, 39, https://doi.org/https://doi.org/10.1029/2012GL053435, 2012.

Ezer, T., Atkinson, L. P., Corlett, W. B., and Blanco, J. L.: Gulf Stream's induced sea level rise and variability along the U.S. mid-Atlantic coast, Journal of Geophysical Research: Oceans, 118, 685–697, https://doi.org/https://doi.org/10.1002/jgrc.20091, 2013.

Fedorov, A. V. and Philander, S. G.: Is El Niño Changing?, Science, 288, 1997–2002, https://doi.org/10.1126/science.288.5473.1997, 2000.

Fedorov, A. V. and Philander, S. G.: A Stability Analysis of Tropical Ocean–Atmosphere Interactions: Bridging Measurements and Theory for El Niño, Journal of Climate, 14, 3086 – 3101, https://doi.org/https://doi.org/10.1175/1520-0442(2001)014<3086:ASAOTO>2.0.CO;2, 2001.

Fereday, D. R., Knight, J. R., Scaife, A. A., Folland, C. K., and Philipp, A.: Cluster Analysis of North Atlantic–European Circulation Types and Links with Tropical Pacific Sea Surface Temperatures, Journal of Climate, 21, 3687 – 3703, https://doi.org/10.1175/2007JCLI1875.1, 2008.

Flandrin, P., Rilling, G., and Goncalves, P.: Empirical mode decomposition as a filter bank, IEEE Signal Processing Letters, 11, 112–114, https://doi.org/10.1109/LSP.2003.821662, 2004.

Frankignoul, C. and Hasselmann, K.: Stochastic climate models, Part II Application to sea-surface temperature anomalies and thermocline variability, Tellus, 29, 289–305, https://doi.org/10.3402/tellusa.v29i4.11362, 1977.

Franzke, C.: Multi-scale analysis of teleconnection indices: climate noise and nonlinear trend analysis, Nonlinear Processes in Geophysics, 16, 65–76, https://doi.org/10.5194/npg-16-65-2009, 2009.

Franzke, C.: Nonlinear Trends, Long-Range Dependence, and Climate Noise Properties of Surface Temperature, Journal of Climate, 25, 4172 – 4183, https://doi.org/10.1175/JCLI-D-11-00293.1, 2012.

Franzke, C. and Woollings, T.: On the Persistence and Predictability Properties of North Atlantic Climate Variability, Journal of Climate, 24, 466 – 472, https://doi.org/10.1175/2010JCLI3739.1, 2011.

Froyland, G., Giannakis, D., Lintner, B., Pike, M., and Slawinska, J.: Spectral analysis of climate dynamics with operator-theoretic approaches, https://doi.org/10.1038/s41467-021-26357-x, 2021.

Ghil, M., Allen, M. R., Dettinger, M. D., Ide, K., Kondrashov, D., Mann, M. E., Robertson, A. W., Saunders, A., Tian, Y., Varadi, F., and Yiou, P.: ADVANCED SPECTRAL METHODS FOR CLIMATIC TIME SERIES, Reviews of Geophysics, 40, 3–1–3–41, https://doi.org/https://doi.org/10.1029/2000RG000092, 2002.

Gilman, D. L., Fuglister, F. J., and Mitchell, J. M.: On the power spectrum of "red noise.", J. Atmos. Sci., 20, 182–184, 1963.

Graham, F. S., Brown, J. N., Wittenberg, A. T., and Holbrook, N. J.: Reassessing Conceptual Models of ENSO, Journal of Climate, 28, 9121 – 9142, https://doi.org/10.1175/JCLI-D-14-00812.1, 2015.

Guilyardi, E., Capotondi, A., Lengaigne, M., Thual, S., and Wittenberg, A. T.: ENSO Modeling, chap. 9, pp. 199–226, American Geophysical Union (AGU), https://doi.org/https://doi.org/10.1002/9781119548164.ch9, 2020.

Hardiman, S. C., Dunstone, N. J., Scaife, A. A., Smith, D. M., Ineson, S., Lim, J., and Fereday, D.: The Impact of Strong El Niño and La Niña Events on the North Atlantic, Geophysical Research Letters, 46, 2874–2883, https://doi.org/https://doi.org/10.1029/2018GL081776, 2019.

Hasselmann, K.: Stochastic climate models Part I. Theory, Tellus, 28, 473–485, https://doi.org/https://doi.org/10.1111/j.2153-3490.1976.tb00696.x, 1976.

Hasselmann, K.: PIPs and POPs: The reduction of complex dynamical systems using principal interaction and oscillation patterns, Journal of Geophysical Research: Atmospheres, 93, 11 015–11 021, https://doi.org/https://doi.org/10.1029/JD093iD09p11015, 1988.

Hu, Z.-Z., Kumar, A., Zhu, J., Huang, B., Tseng, Y.-h., and Wang, X.: On the Shortening of the Lead Time of Ocean Warm Water Volume to ENSO SST Since 2000, Scientific Reports, 7, 4294, https://doi.org/10.1038/s41598-017-04566-z, 2017.

Hu, Z.-Z., Kumar, A., Huang, B., Zhu, J., L'Heureux, M., McPhaden, M. J., and Yu, J.-Y.: The Interdecadal Shift of ENSO Properties in 1999/2000: A Review, Journal of Climate, 33, 4441 – 4462, https://doi.org/10.1175/JCLI-D-19-0316.1, 2020.

Huang, N. E., Shen, Z., Long, S. R., Wu, M. C., Shih, H. H., Zheng, Q., Yen, N.-C., Tung, C. C., and Liu, H. H.: The empirical mode decomposition and the Hilbert spectrum for nonlinear and non-stationary time series analysis, Proceedings of the Royal Society of London. Series A: Mathematical, Physical and Engineering Sciences, 454, 903–995, https://doi.org/10.1098/rspa.1998.0193, 1998.

Huang, N. E., Shen, Z., and Long, S. R.: A NEW VIEW OF NONLINEAR WATER WAVES: The Hilbert Spectrum, Annual Review of Fluid Mechanics, 31, 417–457, https://doi.org/10.1146/annurev.fluid.31.1.417, 1999.

Huang, N. E., Wu, M.-L. C., Long, S. R., Shen, S. S., Qu, W., Gloersen, P., and Fan, K. L.: A confidence limit for the empirical mode decomposition and Hilbert spectral analysis, Proceedings of the Royal Society of London. Series A: Mathematical, Physical and Engineering Sciences, 459, 2317–2345, https://doi.org/10.1098/rspa.2003.1123, 2003.

Jajcay, N., Kravtsov, S., Sugihara, G., Tsonis, A. A., and Paluš, M.: Synchronization and causality across time scales in El Nño Southern Oscillation, npj Climate and Atmospheric Science, 1, 33, https://doi.org/10.1038/s41612-018-0043-7, 2018.

Jenney, A. M., Randall, D. A., and Barnes, E. A.: Quantifying Regional Sensitivities to Periodic Events: Application to the MJO, Journal of Geophysical Research: Atmospheres, 124, 3671–3683, https://doi.org/https://doi.org/10.1029/2018JD029457, 2019.

Jiang, N., Neelin, J. D., and Ghil, M.: Quasi-quadrennial and quasi-biennial variability in the equatorial Pacific, Climate Dynamics, 12, 101–112, https://doi.org/10.1007/BF00223723, 1995.

Jiménez-Esteve, B. and Domeisen, D. I. V.: Nonlinearity in the tropospheric pathway of ENSO to the North Atlantic, Weather and Climate Dynamics, 1, 225–245, https://doi.org/10.5194/wcd-1-225-2020, 2020.

Jiménez-Esteve, B. and Domeisen, D. I. V.: The Tropospheric Pathway of the ENSO–North Atlantic Teleconnection, Journal of Climate, 31, 4563 – 4584, https://doi.org/10.1175/JCLI-D-17-0716.1, 2018.

Jin, F.-F.: An Equatorial Ocean Recharge Paradigm for ENSO. Part I: Conceptual Model, Journal of the Atmospheric Sciences, 54, 811 – 829, https://doi.org/10.1175/1520-0469(1997)054<0811:AEORPF>2.0.CO;2, 1997a.

Jin, F.-F.: An Equatorial Ocean Recharge Paradigm for ENSO. Part II: A Stripped-Down Coupled Model, Journal of the Atmospheric Sciences, 54, 830 – 847, https://doi.org/10.1175/1520-0469(1997)054<0830:AEORPF>2.0.CO;2, 1997b.

Kao, H.-Y. and Yu, J.-Y.: Contrasting Eastern-Pacific and Central-Pacific Types of ENSO, Journal of Climate, 22, 615 – 632, https://doi.org/10.1175/2008JCLI2309.1, 2009.

Keenlyside, N. S., Latif, M., and Dürkop, A.: On Sub-ENSO Variability, Journal of Climate, 20, 3452 – 3469, https://doi.org/10.1175/JCLI4199.1, 2007.

Kim, K.-Y., O'Brien, J. J., and Barcilon, A. I.: The Principal Physical Modes of Variability over the Tropical Pacific, Earth Interactions, 7, 1 – 32, https://doi.org/10.1175/1087-3562(2003)007<0001:TPPMOV>2.0.CO;2, 2003.

Kolotkov, D. Y., Anfinogentov, S. A., and Nakariakov, V. M.: Empirical mode decomposition analysis of random processes in the solar atmosphere, Astronomy & Astrophysics, 592, A153, https://doi.org/10.1051/0004-6361/201628306, 2016.

Kretschmer, M., Adams, S. V., Arribas, A., Prudden, R., Robinson, N., Saggioro, E., and Shepherd, T. G.: Quantifying causal pathways of teleconnections, Bulletin of the American Meteorological Society, pp. 1 – 34, https://doi.org/10.1175/BAMS-D-20-0117.1, 2021.

Lee, J., Planton, Y. Y., Gleckler, P. J., Sperber, K. R., Guilyardi, E., Wittenberg, A. T., McPhaden, M. J., and Pallotta, G.: Robust Evaluation of ENSO in Climate Models: How Many Ensemble Members Are Needed?, Geophysical Research Letters, 48, e2021GL095 041, https://doi.org/https://doi.org/10.1029/2021GL095041, 2021.

Lee, T. and Ouarda, T. B. M. J.: Prediction of climate nonstationary oscillation processes with empirical mode decomposition, Journal of Geophysical Research: Atmospheres, 116, https://doi.org/https://doi.org/10.1029/2010JD015142, 2011.

L'Heureux, M. L., Levine, A. F. Z., Newman, M., Ganter, C., Luo, J.-J., Tippett, M. K., and Stockdale, T. N.: ENSO Prediction, chap. 10, pp. 227–246, American Geophysical Union (AGU), https://doi.org/https://doi.org/10.1002/9781119548164.ch10, 2020.

Lopez, H. and Kirtman, B. P.: WWBs, ENSO predictability, the spring barrier and extreme events, Journal of Geophysical Research: Atmospheres, 119, 10,114–10,138, https://doi.org/https://doi.org/10.1002/2014JD021908, 2014.

Lopez, H., Kirtman, B. P., Tziperman, E., and Gebbie, G.: Impact of interactive westerly wind bursts on CCSM3, Dynamics of Atmospheres and Oceans, 59, 24–51, https://doi.org/https://doi.org/10.1016/j.dynatmoce.2012.11.001, 2013.

Madden, R. A. and Julian, P. R.: Detection of a 40–50 Day Oscillation in the Zonal Wind in the Tropical Pacific, Journal of Atmospheric Sciences, 28, 702 – 708, https://doi.org/10.1175/1520-0469(1971)028<0702:DOADOI>2.0.CO;2, 1971.

Mariotti, A., Ruti, P. M., and Rixen, M.: Progress in subseasonal to seasonal prediction through a joint weather and climate community effort, npj Climate and Atmospheric Science, 1, https://doi.org/10.1038/s41612-018-0014-z, 2018.

Mariotti, A., Baggett, C., Barnes, E. A., Becker, E., Butler, A., Collins, D. C., Dirmeyer, P. A., Ferranti, L., Johnson, N. C., Jones, J., Kirtman, B. P., Lang, A. L., Molod, A., Newman, M., Robertson, A. W., Schubert, S., Waliser, D. E., and Albers, J.: Windows of Opportunity for Skillful Forecasts Subseasonal to Seasonal and Beyond, Bulletin of the American Meteorological Society, 101, E608 – E625, https://doi.org/https://doi.org/10.1175/BAMS-D-18-0326.1, 2020.

Penland, C. and Sardeshmukh, P. D.: The Optimal Growth of Tropical Sea Surface Temperature Anomalies, Journal of Climate, 8, 1999 – 2024, https://doi.org/10.1175/1520-0442(1995)008<1999:TOGOTS>2.0.CO;2, 1995.

Philander, S. G. H.: El Niño, La Niña, and the southern oscillation, Academic Press, Inc., San Diego, California, 1990.

Picaut, J., Masia, F., and du Penhoat, Y.: An Advective-Reflective Conceptual Model for the Oscillatory Nature of the ENSO, Science, 277, 663–666, https://doi.org/10.1126/science.277.5326.663, 1997.

Planton, Y. Y., Guilyardi, E., Wittenberg, A. T., Lee, J., Gleckler, P. J., Bayr, T., McGregor, S., McPhaden, M. J., Power, S., Roehrig, R., Vialard, J., and Voldoire, A.: Evaluating Climate Models with the CLIVAR 2020 ENSO Metrics Package, Bulletin of the American Meteorological Society, 102, E193 – E217, https://doi.org/10.1175/BAMS-D-19-0337.1, 2021.

Qian, C., Wu, Z., Fu, C., and Wang, D.: On Changing El Niño: A View from Time-Varying Annual Cycle, Interannual Variability, and Mean State, Journal of Climate, 24, 6486 – 6500, https://doi.org/10.1175/JCLI-D-10-05012.1, 2011.

Rayner, N. A., Parker, D. E., Horton, E. B., Folland, C. K., Alexander, L. V., Rowell, D. P., Kent, E. C., and Kaplan, A.: Global analyses of sea surface temperature, sea ice, and night marine air temperature since the late nineteenth century, Journal of Geophysical Research, 108, D14, 4407, https://doi.org/10.1029/2002JD002670, 2003.

Rehman, N. and Mandic, D. P.: Multivariate empirical mode decomposition, Proceedings of the Royal Society A: Mathematical, Physical and Engineering Sciences, 466, 1291–1302, https://doi.org/10.1098/rspa.2009.0502, 2010.

Rehman, N. and Mandic, D. P.: Filter Bank Property of Multivariate Empirical Mode Decomposition, IEEE Transactions on Signal Processing, 59, 2421–2426, https://doi.org/10.1109/TSP.2011.2106779, 2011.

Rilling, G., Flandrin, P., and Gonçalves, P.: On empirical mode decomposition and its algorithms, in: Proceedings of IEEE-EURASIP Workshop on Nonlinear Signal and Image Processing NSIP-03, Grado, Italy, https://hal.inria.fr/inria-00570628, 2003.

Rilling, G., Flandrin, P., Goncalves, P., and Lilly, J. M.: Bivariate Empirical Mode Decomposition, IEEE Signal Processing Letters, 14, 936–939, https://doi.org/10.1109/LSP.2007.904710, 2007.

Roulston, M. S. and Neelin, J. D.: The response of an ENSO Model to climate noise, weather noise and intraseasonal forcing, Geophysical Research Letters, 27, 3723–3726, https://doi.org/https://doi.org/10.1029/2000GL011941, 2000.

Runge, J., Petoukhov, V., Donges, J. F., Hlinka, J., Jajcay, N., Vejmelka, M., Hartman, D., Marwan, N., Paluš, M., and Kurths, J.: Identifying causal gateways and mediators in complex spatio-temporal systems, Nature Communications, 6, 8502, https://doi.org/10.1038/ncomms9502, 2015.

Singh, A. and Delcroix, T.: Eastern and Central Pacific ENSO and their relationships to the recharge/discharge oscillator paradigm, Deep Sea Research Part I: Oceanographic Research Papers, 82, 32–43, https://doi.org/https://doi.org/10.1016/j.dsr.2013.08.002, 2013.

Slawinska, J. and Giannakis, D.: Indo-Pacific Variability on Seasonal to Multidecadal Time Scales. Part I: Intrinsic SST Modes in Models and Observations, Journal of Climate, 30, 5265 – 5294, https://doi.org/10.1175/JCLI-D-16-0176.1, 2017.

Stallone, A., Cicone, A., and Materassi, M.: New insights and best practices for the successful use of Empirical Mode Decomposition, Iterative Filtering and derived algorithms, Scientific Reports, 10, 15 161, https://doi.org/10.1038/s41598-020-72193-2, 2020.

Stein, K., Schneider, N., Timmermann, A., and Jin, F.-F.: Seasonal Synchronization of ENSO Events in a Linear Stochastic Model, Journal of Climate, 23, 5629 – 5643, https://doi.org/10.1175/2010JCLI3292.1, 2010.

Suarez, M. J. and Schopf, P. S.: A Delayed Action Oscillator for ENSO, Journal of Atmospheric Sciences, 45, 3283 – 3287, https://doi.org/10.1175/1520-0469(1988)045<3283:ADAOFE>2.0.CO;2, 1988.

Timmermann, A., An, S. I., Kug, J. S., Jin, F. F., Cai, W., Capotondi, A., Cobb, K. M., Lengaigne, M., McPhaden, M. J., Stuecker, M. F., Stein, K., Wittenberg, A. T., Yun, K. S., Bayr, T., Chen, H. C., Chikamoto, Y., Dewitte, B., Dommenget, D., Grothe, P., Guilyardi, E., Ham, Y. G., Hayashi, M., Ineson, S., Kang, D., Kim, S., Kim, W., Lee, J. Y., Li, T., Luo, J. J., McGregor, S., Planton, Y., Power, S., Rashid, H., Ren, H. L., Santoso, A., Takahashi, K., Todd, A., Wang, G., Wang, G., Xie, R., Yang, W. H., Yeh, S. W., Yoon, J., Zeller, E., and Zhang, X.: El Nino-Southern Oscillation complexity, Nature, 559, 535–545, https://doi.org/10.1038/s41586-018-0252-6, 2018.

Wang, B. and An, S.-I.: Why the properties of El Niño changed during the late 1970s, Geophysical Research Letters, 28, 3709–3712, https://doi.org/https://doi.org/10.1029/2001GL012862, 2001.

Wang, C.: A Unified Oscillator Model for the El Niño-Southern Oscillation, Journal of Climate, 14, 98 – 115, https://doi.org/10.1175/1520-0442(2001)014<0098:AUOMFT>2.0.CO;2, 2001.

Wang, C.: A review of ENSO theories, National Science Review, 5, 813–825, https://doi.org/10.1093/nsr/nwy104, 2018.

Wang, C. and Fiedler, P. C.: ENSO variability and the eastern tropical Pacific: A review, Progress in Oceanography, 69, 239–266, https://doi.org/https://doi.org/10.1016/j.pocean.2006.03.004, a Review of Eastern Tropical Pacific Oceanography, 2006.

Wang, C., Weisberg, R. H., and Virmani, J. I.: Western Pacific interannual variability associated with the El Niño-Southern Oscillation, Journal of Geophysical Research: Oceans, 104, 5131–5149, https://doi.org/https://doi.org/10.1029/1998JC900090, 1999.

Wang, R. and Ren, H.-L.: Understanding Key Roles of Two ENSO Modes in Spatiotemporal Diversity of ENSO, Journal of Climate, 33, 6453 – 6469, https://doi.org/10.1175/JCLI-D-19-0770.1, 2020.

865 Weisberg, R. H. and Wang, C.: A Western Pacific Oscillator Paradigm for the El Niño-Southern Oscillation, Geophysical Research Letters, 24, 779–782, https://doi.org/https://doi.org/10.1029/97GL00689, 1997.

Wengel, C., Latif, M., Park, W., Harlaß, J., and Bayr, T.: Seasonal ENSO phase locking in the Kiel Climate Model: The importance of the equatorial cold sea surface temperature bias, Climate Dynamics, 50, 901–919, https://doi.org/10.1007/s00382-017-3648-3, 2018.

Wittenberg, A. T.: Extended Wind Stress Analyses for ENSO, Journal of Climate, 17, 2526 – 2540, https://doi.org/10.1175/1520-
870 0442(2004)017<2526:EWSAFE>2.0.CO;2, 2004.

Wu, Z. and Huang, N. E.: A study of the characteristics of white noise using the empirical mode decomposition method, Proceedings of the Royal Society of London. Series A: Mathematical, Physical and Engineering Sciences, 460, 1597–1611, https://doi.org/10.1098/rspa.2003.1221, 2004.

Wu, Z. and Huang, N. E.: ENSEMBLE EMPIRICAL MODE DECOMPOSITION: A NOISE-ASSISTED DATA ANALYSIS METHOD,
875 Advances in Adaptive Data Analysis, 01, 1–41, https://doi.org/10.1142/S1793536909000047, 2009.

Wu, Z., Huang, N. E., Long, S. R., and Peng, C.-K.: On the trend, detrending, and variability of nonlinear and nonstationary time series, Proceedings of the National Academy of Sciences, 104, 14 889–14 894, https://doi.org/10.1073/pnas.0701020104, 2007.

Zhang, Z., Ren, B., and Zheng, J.: A unified complex index to characterize two types of ENSO simultaneously, Scientific Reports, 9, 8373, https://doi.org/10.1038/s41598-019-44617-1, 2019.